Acta Materialia 259 (2023) 119239

Contents lists available at ScienceDirect

Acta Materialia

journal homepage: www.elsevier.com/locate/actamat

Full length article

Amorphous-crystalline nanostructured Nd-Fe-B permanent magnets using laser powder bed fusion: Metallurgy and magnetic properties

Julan Wu [a,*], Nesma T. Aboulkhair [a,b], Stuart Robertson [c], Zhaoxia Zhou [c], Paul A.J. Bagot [d], Michael P. Moody [d], Michele Degano [e], Ian Ashcroft [a], Richard J.M. Hague [a]

[a] Centre for Additive Manufacturing, Faculty of Engineering, University of Nottingham, Nottingham NG8 1BB, UK
[b] Additive Manufacturing Group, Advanced Materials Research Centre (AMRC), Technology Innovation Institute (TII), Masdar City, Abu Dhabi, P.O.Box 9636, United Arab Emirates
[c] Loughborough Materials Characterisation Centre, Department of Materials, Loughborough University, Loughborough LE11 3TU, UK
[d] Department of Materials, University of Oxford, Oxford OX1 3PH, UK
[e] Power Electronics, Machines and Control Group, Faculty of Engineering, University of Nottingham, Nottingham NG7 2RD, UK

ARTICLE INFO

Keywords:
Additive manufacturing (AM)
Laser powder bed fusion (PBF-LB)
Permanent magnet
Nd-Fe-B, Functional material
Atom probe tomography (APT)

ABSTRACT

Laser powder-bed fusion (PBF-LB), a class of additive manufacturing (AM), has attracted wide interest in the production of Nd-Fe-B permanent magnets, benefiting from the minimisation of waste of rare-earth elements and the post-processing requirements. Most research on PBF-LB Nd-Fe-B has focused on reducing defects in printed parts alongside the improvement of the resultant magnetic properties. Detailed analysis of the microstructure that results in permanent magnetic properties is yet to be published. In this research, a combination of high-resolution microstructural investigations was conducted for this purpose. For the first time, an in-depth analysis of the grain structure in terms of morphology, size distribution, and texture is presented and correlated to the permanent magnetic performance. Melt pools showed a hierarchical grain size distribution of primary $Nd_2Fe_{14}B$ phase grains with a polygonal morphology and random crystalline alignment, in addition to a small amount of Nd-rich and Nd-lean precipitates in the matrix of the Ti-rich amorphous grain boundaries. The permanent magnetic properties of this material are mainly determined by the nanostructured $Nd_2Fe_{14}B$ grains and the amorphous Ti-rich iron-based intergranular phase but could be weakened by precipitates that act as magnetic pores. Remelting during PBF-LB led to the transformation of the coarse grains of the previously solidified layer to fine ones, favourable for the permanent magnetic properties. The mechanisms of these complex phase formations and transformations during processing and the development of the nanocrystalline microstructure are elucidated in this paper as a basis for informing the optimisation process for microstructural development.

1. Introduction

Since their discovery, Nd-Fe-B magnets have attracted significant interest for their outstanding magnetic performance, being widely used in electronics, appliances, automotive, energy systems, and medical devices, to name a few. [1–4]. Microcrystalline and nanocrystalline Nd-Fe-B powders are usually used as feedstock material to produce sintered or bonded (mixed with binders) magnets [5–10]. Sintered magnets can be anisotropic by pre-aligning the powder before sintering, which yields a remanence twice that of isotropic magnets, according to the Stoner-Wohlfrarth model [11]. The high magnetic properties of sintered magnets are due to their unique composite-like structure, having a continuous rare earth element (RE)-rich film surrounding the grain boundaries (GBs), thanks to the relatively high RE concentration (~14–15%) [1,12,13]. Micro-scale grains are decoupled by the RE-rich phase at the GBs [14–17], which minimises the magnetic coupling between the grains. As for the bonded Nd-Fe-B, the corrosion resistance and ductility surpasses those of the sintered ones, thanks to the polymeric binder protecting the magnetic powder [18,19]. However, the binders also reduce the metallic phase density to 60–80 vol.% [18–21] resulting in lower magnetic density compared to sintered ones [18]. The poor temperature resistance of many engineering polymers also limits the operating temperature of the polymer-bonded magnets [1,19]. Further, the machining of conventionally manufactured magnets is

* Corresponding author.
E-mail address: julan.wu@nottingham.ac.uk (J. Wu).

https://doi.org/10.1016/j.actamat.2023.119239
Received 27 January 2023; Received in revised form 4 August 2023; Accepted 8 August 2023
Available online 10 August 2023
1359-6454/© 2023 The Authors. Published by Elsevier Ltd on behalf of Acta Materialia Inc. This is an open access article under the CC BY license (http://creativecommons.org/licenses/by/4.0/).

usually needed to achieve the required geometries and dimensions for specific applications. However, being a brittle material at room temperature, it is susceptible to machining defects [1] with the machined swarf material also requiring more energy to recycle/recover the RE element for future use. Owing to the strength of this magnetic material and the disadvantages of its conventional manufacturing processes, themes of research and development for the Nd-Fe-B magnets include improvements in their maximum energy product, environmental stability and corrosion resistance, near-net-shape manufacture, and magnetization behaviour [1].

Additive manufacturing (AM) methods have been widely demonstrated for the production of net-shape or near-net-shape magnets, reducing raw material wastage through the avoidance or minimisation of post-process machining [20–29]. Extrusion-based methods [22,23], electron beam melting (EBM) [20,24], laser powder bed fusion (PBF-LB) [25–28], selective laser sintering (SLS) [30], and stereolithography (SLA) [29] are AM techniques that have been investigated for the production of Nd-Fe-B parts. The magnetic properties, corrosion resistance, and ductility of the isotropic bonded Nd-Fe-B magnets produced by extrusion-based AM are comparable to their conventionally bonded counterparts [22,23,31]. Although the Nd-Fe-B parts fabricated via EBM were fully metallic, their magnetic properties fell short of expectations due to unfavourable phases forming during fabrication [20]. Their remanence was less than 0.1 T, which is significantly lower than the 0.73–0.76 T of the MQP-S feedstock material [32]. As-printed SLS magnets showed significantly lower remanence (0.436 T) and comparable coercivity (0.653 T) compared to their PBF-LB counterparts (0.650 T and 0.603T, respectively) due to the lower relative density of the former [29,30]. However, the coercivity of the former was enhanced to 1.518 T via post-process metal infiltration by Nd-rich alloys with low melting point [30], but the remanence dropped to 0.390 T(significantly lower than the state-of-the-art of PBF-LB magnets). So far, PBF-LB Nd-Fe-B magnets offer the best permanent magnetic properties, structural design freedom, and temperature resistance of all the various AM processes.

Magnequench MQP-S, with the chemical composition of $Nd_{7.5}Pr_{0.7}Zr_{2.6}Ti_{2.5}Co_{2.5}Fe_{75}B_{88,}$ is a RE-lean alloy with only 8.2 at% RE; this is lower than the theoretical percentage of Nd required to form the $Nd_2Fe_{14}B$ phase and far lower than the feedstock material usually used in conventional sintering (14–18%). Owing to its unique spherical morphology and suitable particle size distribution, the powder has been widely used in PBF-LB studies [25–28,33]. During PBF-LB, the feedstock powder is nearly fully melted and re-crystallized during cooling down and solidification. The PBF-LB process parameters (e.g. laser power, scan speed, hatch distance) influence the relative density of the produced parts [25–28,33], which in turn affects the magnetic properties [26,27]. Bittner et al. [27] reported a remanence improvement of ~21% through a parametric study of process parameters. The magnetic properties of the PBF-LB material are expected to be dependant on the microstructure. The rapid solidification rate in PBF-LB is similar to melt-spinning, which is a common method to produce Nd-Fe-B ribbons, where the magnetic properties are strongly related to the microstructure, which in turn is dependant on the thermal history during processing [34]. In PBF-LB, the thermal history includes additional remelting and *in-situ* heat treatment of neighbouring hatches and underlying layers.

Despite the numerous studies focussed on PBF-LB of Nd-Fe-B, there has not previously been a comprehensive study on these parts' microstructure from the perspective of the density of the magnetic phase $Nd_2Fe_{14}B$, the grain size, the alignment of the grains and the morphology of the GBs that govern the permanent magnetic properties [14–17,35–37]. To comprehensively correlate the process-structure-property relationship of PBF-LB, this paper presents a detailed microstructural study, which is critical for obtaining the maximum energy product of the permanent magnets. Moreover, the formation of the material during the process and the process-structure-property relationships are discussed.

2. Materials and methods

A commercial Renishaw AM125 (UK) PBF-LB system was used to produce the Nd-Fe-B samples in this study. The system is equipped with a 200 W yttrium fibre laser with a spot size of 40 μm operating in a pulsed mode. The feedstock powder, MQP-S-11–9–20,001, was acquired from Magnequench (Germany). The powder was stored in sealed bottles before use and the specimens, fabricated under argon, were stored in vacuumed bags to minimise oxidation. For the metallographic study, cylindrical samples of 10 mm diameter and 10 mm height were produced. A single track was deposited on the top of the cylindrical sample, which was used to study the microstructure forming during PBF-LB without the effect of remelting/*in-situ* heat treatment from the neighbouring tracks within the same layer or from the subsequent layers. The Nd-Fe-B samples were processed by an optimised parameter combination, published in our earlier work [28]. The process parameters employed were: a layer thickness of 30 μm, a point distance of 65 μm, an exposure time of 72 μs, a hatch distance of 100 μm, and a bi-directional scan strategy with a rotation of 67° between layers.

For metallographic preparation, the samples were cross-sectioned and polished using standard metallographic techniques to a 1 μm finish. Following conventional polishing, the samples were vibro-polished to a 0.03 μm finish using a Buehler Vibromet polisher (Buehler, Illinois, United States) with a non-crystallizing colloidal silica polishing suspension. Phase identification was performed by collecting X-ray diffraction (XRD) patterns from the loose MQP-S powder and the polished specimens using a Bruker D8 Advance Da Vinci (Bruker, Mass achusetts, United States) with a step size of 0.01° and an exposure time of 10 s at each step. The microstructure of the polished Nd-Fe-B samples was studied using an FEI G4 CXe plasma focussed ion beam (pFIB) scanning electron microscope (SEM) (FEI, Oregon, United States) in the back-scatter electron (BSE) mode. Electron backscattered diffraction (EBSD) patterns coupled with energy dispersive X-ray spectroscopy (EDS) mapping with a step size of 0.1 μm were obtained using NordlysMax3 EBSD detector (Oxford Instruments, Oxon, UK) and X-max 150 EDS detector (Oxford Instruments, Oxon, UK), on a JEOL-7100F-field emission gun (FEG) – scanning electron microscope (SEM) (JEOL, Tokyo, Japan) at an accelerating voltage of 15 kV. The software AZTec and AZTec Crystal were used to process the data.

Given the extremely fine and complex microstructure of the material, transmission electron microscopy (TEM) and atom probe tomography (APT) were utilised to study the metallurgy of the printed samples. Samples for TEM and APT were prepared using a plasma focused ion beam (pFIB) on an FEI G4 Cxe pFIB-SEM (FEI, Oregon, United States) to lift out and polish a thin lamella from the region of interest across the melt pool boundary for the former and needles from various regions within the melt pool for the latter. The specific locations of the TEM lamella and APT needles are shown in Fig. 1. TEM imaging was performed using a FEI Tecnai F20 G2 S – Twin FEG-scanning TEM (TEM), equipped with an EDS X-Max 80 mm^2 TLE detector (Oxford Instruments, Oxon, UK). Further, high-resolution TEM (HR-TEM) was used to study the finer details of the microstructure of the investigated samples and collect selective area diffraction (SAD) patterns. The APT study was performed on the needles using a LEAP™ 3000X HR (CAMECA, Gennevilliers, France).

SEM and TEM micrographs were used to obtain the sizes of the grains and dendrites using 'line measure' function in the image analysis software, ImageJ [38]. On each micrograph, at least fifty measurements of diameters or lengths and widths of the primary grains and the dendrites were taken at random locations. A comparison was made between the range and average sizes of the grains and dendrites at distinctive locations within the melt pools.

To measure the magnetic properties of the as-printed samples and correlate them to the investigated microstructure, induction

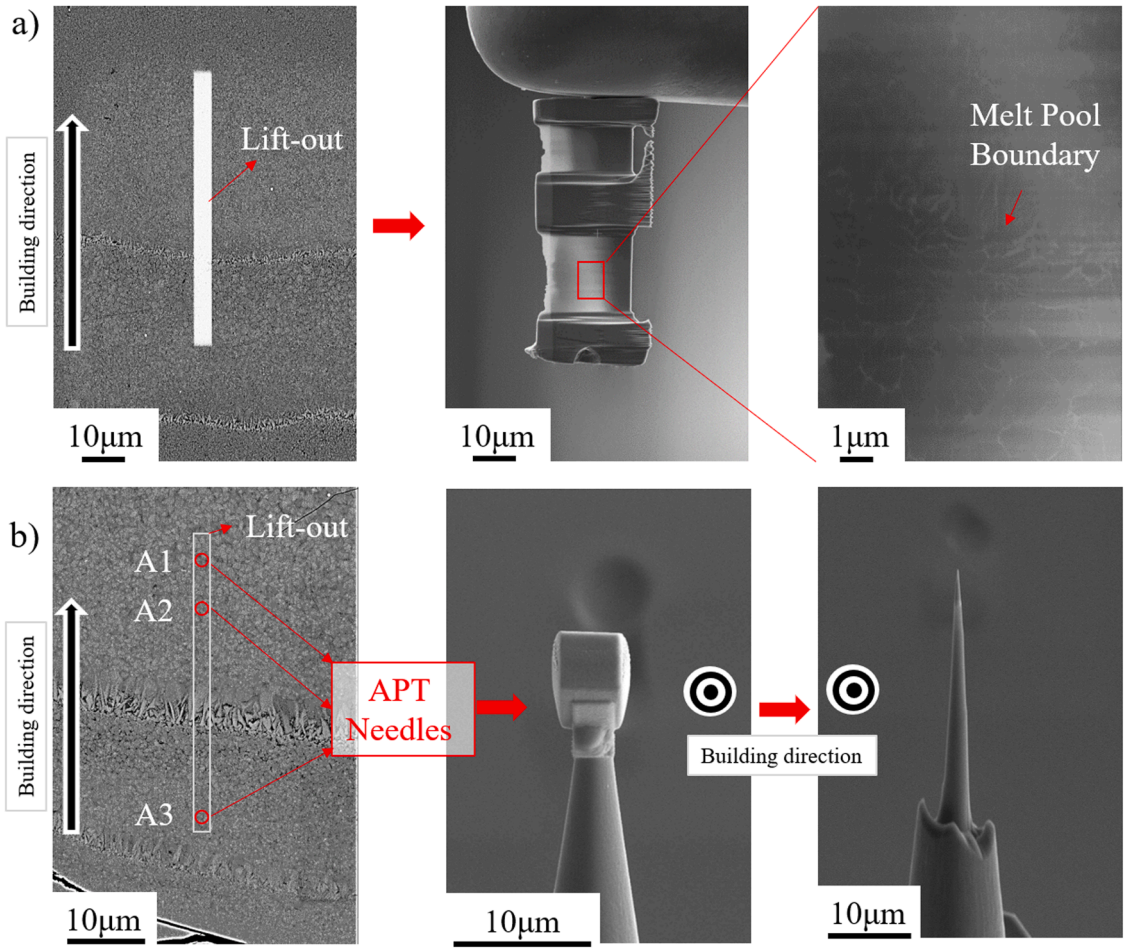

Fig. 1. pFIB was used to prepare TEM and APT samples from the as-printed PBF-LB Nd-Fe-B to lift out (a) a lamella for TEM analysis and (b) needles for APT analysis.

demagnetisation curves were collected by a NIM-2000H closed-circuit hysteresigraph after magnetization in a 2T external magnetic field using a pulse magnetizer NIM-10,000 (National Institute of Metrology, Beijing, China). The tested specimens were cylindrical samples of 10 mm diameter and 10 mm height. In order to study the temperature effect on the characteristics of the permanent magnet (remanence (B_r) and coercivity (H_c)), each sample was measured at various temperatures: ambient (20°), 50 °C, 100 °C, 150 °C, and 200 °C. The samples were magnetized using the pulse magnetizer before measuring at each temperature to ensure magnetic saturation in the permanent magnetic samples. The accuracy of the measurements was established to be ±1%.

3. Results and discussion

3.1. The hierarchical grain structure in PBF-LB Nd-Fe-B

The cross-sections of the as-printed samples revealed a microstructure consisting of overlapping melt pools with fish-scale-like melt pool boundaries in-between. A representative region studied using SEM and EBSD is illustrated schematically in Fig. 2(a) according to the SEM micrograph in Fig. 2(b). The fish-scale-like microstructure can be seen in Fig. 2(b) with columnar grains at the melt pool boundaries and irregular polygonal grains within the melt pool area, depicted in the higher magnification images (c) and (d). The layer-by-layer nature of the manufacturing process leads to repetitive thermal cycles experienced by the material. This resulted in a gradient change in grain size along the depth of each melt pool, i.e. parallel to the build direction (Fig. 2(c)). The size of the equiaxed polygonal grains within the melt pool core ranged from 0.2 to 2 μm (Fig. 2(c)). In principle, the gradient grain size within each melt pool is dictated by the thermal gradients experienced during processing. As has been established in the literature, materials processed by PBF-LB that result in a fish-scale-like microstructure are characterised by finer equiaxed grains in the melt pool core at the upper regions with coarser elongated grains at the boundaries of the melt pools, following the direction of a thermal gradient, i.e. towards the heat source [39–41]. This agrees with the microstructure reported in this study. Nevertheless, at the top of each melt pool, between each two adjacent melt pools along the build direction, a region of coarser equiaxed grains was observed (Fig. 2(c), (d), and (e)), where the grain size was measured to be 1.3 mm on average. Below this, finer equiaxed grains were observed, with an average grain size of 0.4 mm (Fig. 2(c), (d), and (f)). The columnar elongated grains at the melt pool boundaries (Fig. 2(d)) were around 2 μm long and 0.4 μm wide. A similar grain morphology transition from columnar to equiaxed grains within the melt pool has been reported for Zr-modified Al alloys [42]. The added element (Zr) serves as a nucleation site during solidification, promoting heterogeneous nucleation. An equiaxed grain structure was also observed in $Fe_6NiCoCrAlTiSi$ high-entropy alloy coatings produced via laser cladding [43]. This suggests that equiaxed grain formation could be driven by the characteristic element composition of the MQP-S powder ($Nd_{7.5}Pr_{0.7}Zr_{2.6}Ti_{2.5}Co_{2.5}Fe_{75}B_{88}$) used in this study.

Livingston [44] calculated the maximum size of a grain to be single domain as 0.3 μm, which means that larger grains are expected to be multi-domain. The magnetic properties produced by multi-domain grains are inferior to single-domain grains due to the coupling effect between the domains within the former. In the PBF-LB Nd-Fe-B magnets, grains larger than 0.3 μm are therefore classed as multi-domain, with lower demagnetization resistance, and consequently lower coercivity.

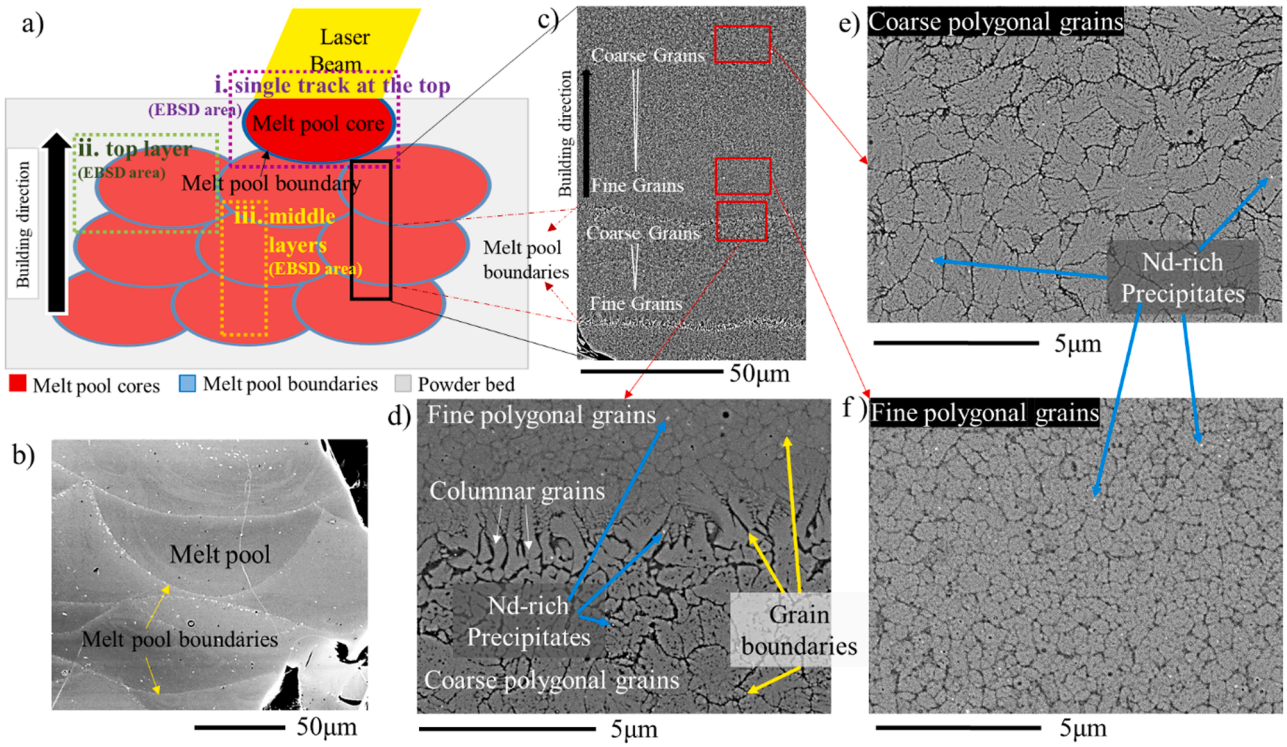

Fig. 2. Microstructure of the PBF-LB Nd-Fe-B. (a) Schematic illustration of the formation of the melt pools during the PBF-LB process as well as the area being studied using SEM and EBSD in this work. (b) SEM micrograph showing the fish-scale-like microstructure along the build direction; (c) SEM micrograph at a lower magnitude showing the repeated gradient change of the grain size along the build direction in the melt pool; (d) SEM micrograph of a representative overlapped region of two adjacent layers, depicted the polygonal grains in the melt pool and the columnar grains at the melt pool boundary; (e) (f) SEM micrographs of the coarse and fine polygonal grains at the top and bottom of a melt pool of the PBF-LB Nd-Fe-B.

Another important aspect is the presence of elongated columnar grains at the melt pool boundaries with high aspect ratios along the build direction. As reported by Sepheri-Amin et al. [45], coercivity decreases with an increasing aspect ratio of the grains due to the lower stray field. PBF-LB magnets with grain sizes between 0.2 and 2 μm have coarser grains compared to magnets fabricated by conventional rapid solidification methods (e.g. melt spun and hot-deformed magnets with average grain sizes of 0.1 and 0.2 μm, respectively). The coupling effect due to coarser grain size and the presence of some columnar grains can be two of the reasons behind the relatively lower permanent magnetic properties in PBF-LB magnets. For enhanced permanent magnetic properties, it is recommended to transform the coarser grains into finer ones by tuning the process parameters. For instance, it has been shown that permanent magnetic properties can be enhanced by reducing the layer thickness [26,46]. Based on the understanding of the PBF-LB process and the solidification kinetics, Jacimovic et al. asserted that melt pools are smaller in thinner powder layers, resulting in faster solidification and finer grains after solidification [26]. The difference in grain size at different areas of the melt pool was also observed in PBF-LB parts made from Nd-Fe-B powder with higher Nd content [47]. Our observations here of the periodic and hierarchical grain structure in each layer, similar to the work of Bittner et al. [33], attributed to gradient temperature within the melt pools during solidification, further explain the mechanism behind this phenomenon considering remelting during PBF-LB. A thinner layer thickness means a larger penetration depth of the laser irradiation leading to more remelting of the originally coarser grains at the upper region of the preceding layer transforming them into finer grains. Consequently, the average grain size of the whole part is refined, in theory, leading to improved magnetic properties. Amorphous-crystalline nanostructure

The TEM-EDS analysis provided a fundamental understanding of the microstructure of the PBF-LB Nd-Fe-B. The chemical elements' distribution within the various regions of a representative melt pool was mapped using TEM-EDS, as shown in Fig. 3. Co, Zr, Pr, Cu, and Ti are added to the formula of the MQP-S powder [48] for enhanced magnetic properties [49–54]. After PBF-LB processing (Fig. 3), Co was evenly distributed within the sample. On the other hand, microscale precipitation of Ti was observed at the GBs within the whole area mapped with Zr segregations at the GBs, mainly within the melt pool boundary; this could be attributed to the thermal expansion and contraction of the melt pool during processing [55,56]. In rapidly solidified alloys, Zr is advantageous for stabilizing the amorphous phases and promoting grain refinement in the crystalline phases [49,57–61]. Zr-rich intergranular phases may also act as pinning centres inhibiting the movement of the domain walls between the grains [49,60]. Pr was dispersed within the melt pool but was depleted from the intergranular phases around the columnar grains at the melt pool boundaries where Zr was more pronounced. Nd was dispersed in the primary grains, besides areas of higher concentrations in the form of globular precipitates (see Table 1 for the quantitative analysis). It is interesting to note that the distribution of Fe varied across the various regions of the melt pool. It was uniformly distributed in the columnar and coarse grain regions in contrast to the subtle reduction at the GBs in the fine grains' region indicating a lesser Fe content, as annotated in Fig. 3.

The respective quantitative analysis is displayed in Table 1. A comparison of the chemical composition of the relatively larger areas at different regions of the melt pool was undertaken in the EDS study, i.e. fine polygonal, columnar, and coarse polygonal grain regions (as annotated in Fig. 3(a) and (c)). As displayed in Table 1, no significant quantitative differences were noted between the three regions of the melt pool. This suggested that the grains with different sizes and morphology at different regions of the melt pool have similar chemical composition. The phase of the primary grains will be studied using other characterisation techniques later in this article. The globular

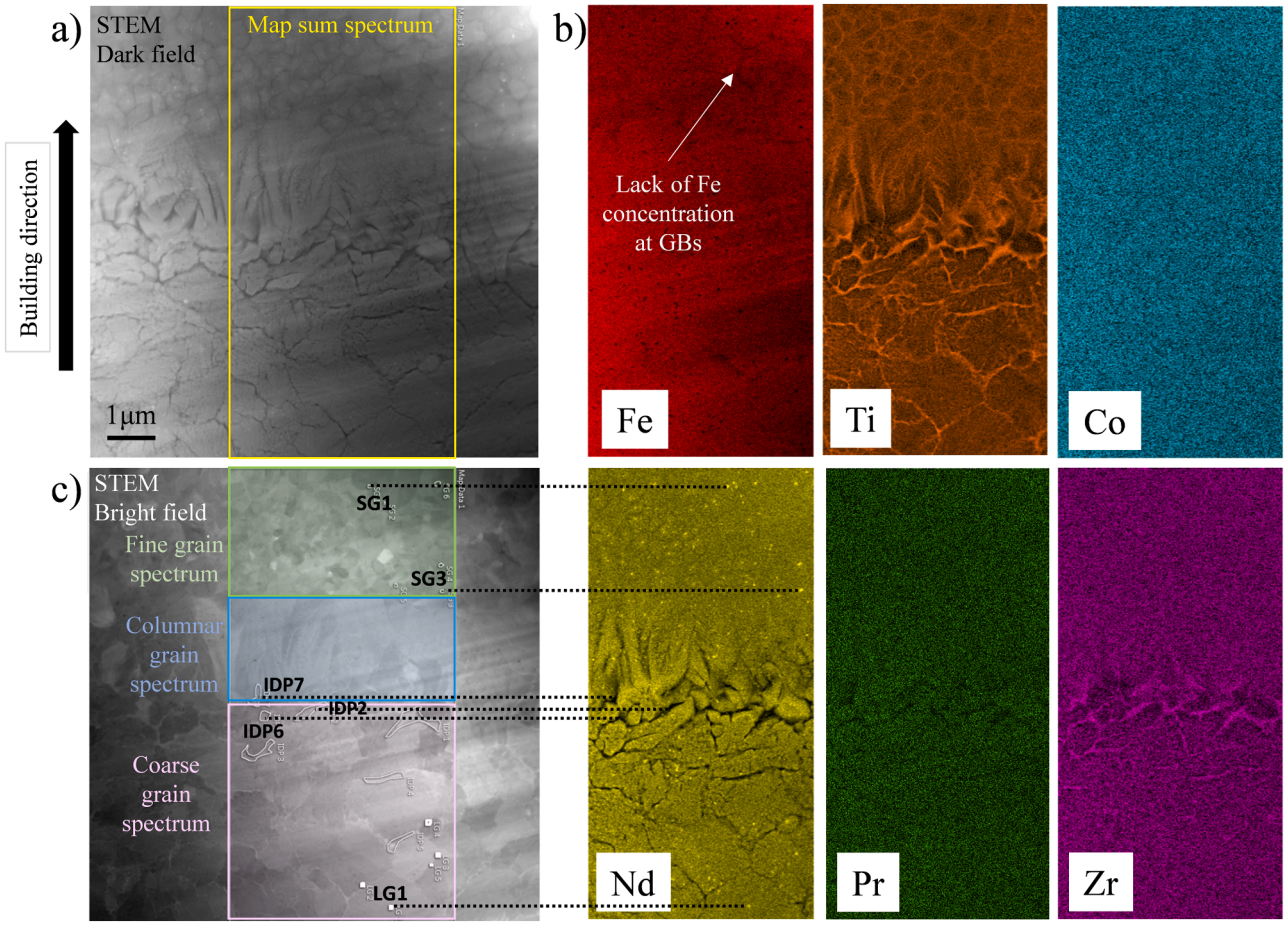

Fig. 3. TEM-EDS mapping of the PBF-LB Nd-Fe-B FIB lamella showing the chemical elements.

Table 1
Chemical compositions from TEM-EDS at the annotated regions in Fig. 3.

At% Map	Fe	Nd	Zr	Pr	Ti	Co	Cu*	B*	ID* (in Fig. 3. c)
Feedstock powder	75.0	7.5	2.6	0.7	2.5	2.5	0.1	8.8	MQP-S datasheet [48]
Whole area mapping	79.1	8.7	2.8	0.9	3.1	3.4	2.0	–	Map sum spectrum
Fine grain area	79.4	8.7	2.9	0.9	3.1	3.4	1.6	–	Fine grain spectrum
Melt-pool boundary	79.2	8.6	2.9	0.9	3.1	3.4	2.0	–	Columnar grain spectrum
Large grain area	79.0	8.6	2.8	0.9	3.0	3.3	2.2	–	Large grain spectrum
Nd-rich precipitate regions	72.2	16.6	1.8	2.2	2.0	3.2	1.9	–	SG3
	71.7	16.6	2.3	2.0	2.3	2.8	2.1	–	SG1
	71.7	16.6	2.3	2.0	2.3	2.8	2.1	–	LG1
Ti-rich precipitate regions	79.2	5.1	4.2	0.5	5.6	3.4	1.9	–	IDF2
	79.8	3.9	4.5	0.3	6.0	3.5	1.9	–	IDF7
	79.3	4.8	4.3	0.5	5.7	3.5	2.0	–	IDF6

* (1) The TEM data will have a higher copper content as the sample is on a copper grid, which results in a copper background from the milling of the sample.
(2) Quantitative TEM-EDS analysis of Boron (B) when associated with other light elements can be challenging [62] and potentially unreliable especially in trace concentrations. In this case boron was not included in the characterisation.
(3) The area of the map in TEM-EDS was manually drawn, and more accurate quantitative chemical compositions of the precipitates and the primary grains are displayed in the Atom probe tomography (APT) results in this research.

precipitates and the intergranular precipitates are annotated on the maps and EDS data was collected from them. The EDS analysis (Table 1) on the precipitates confirmed that significantly higher composition of the rare-earth element Nd and Pr concentrated at the globular precipitates. In addition, Ti was abundant in the intergranular phase. However, owing to the nanoscale nature of these precipitates, a more accurate quantitative chemical analysis of them was conducted using atom probe tomography (APT), which is presented later in this article.

The rapid melting and solidification rates associated with PBF-LB are known to lead to the formation of extremely fine microstructures that in some cases, like with Nd-Fe-B, can even yield nanocrystalline features. Therefore, transmission electron microscopy (TEM) was utilised to further study the metallurgy of the as-printed samples. The three characteristic regions that constitute each melt pool can be seen in Fig. 4 where the fine polygonal, columnar, and coarse polygonal grains are presented in (a, b), (c, d), and (e, f), respectively. The sizes of the grains

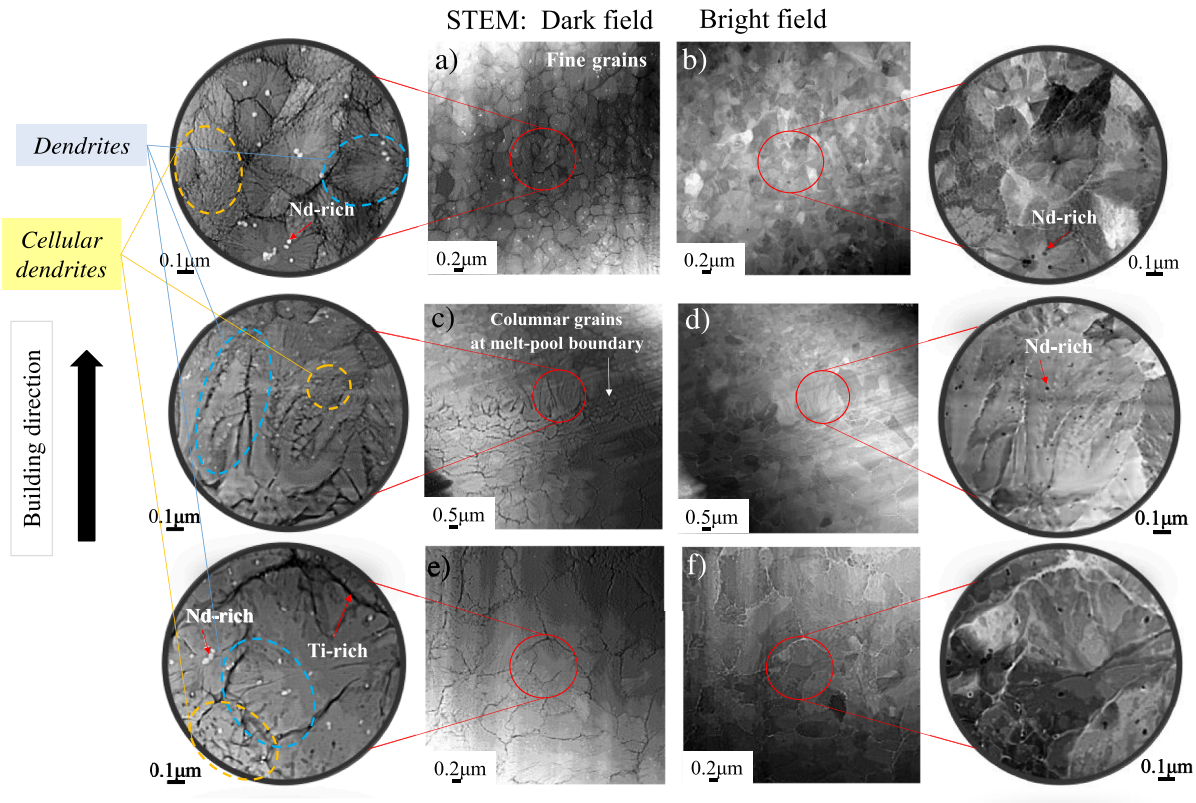

Fig. 4. TEM images of the PBF-LB Nd-Fe-B FIB lamella. (a, b) the fine grains at the bottom of the melt pool were polygonal with and disconnected by the intergranular phases. Small amounts of the Nd-rich precipitates were observed. (c, d) Columnar dendrites were observed at the melt pool boundaries. (e, f) showing the large grains at the top of the melt pool with polygonal morphologies and dislocations.

were measured from the SEM images (Fig. 2). Dendrites were observed both in the polygonal grains in the melt pool core and the columnar grains at the melt pool boundaries, as annotated in Fig. 4. The columnar dendrites were formed at the melt pool boundaries determined by the constitutional undercooling of the melt at their tips, due to the undercooling along the thermal gradient direction during laser processing. The dendrites within the grains were measured from the TEM images (Fig. 4) at higher magnification. The presence of the dendritic structures with their sizes in the nano-scale range (23.1 ± 9.6 nm in width and 119.9 ± 42.0 nm in length within the fine region, 54.7 ± 22.4 nm in width and 1147.7 ± 453.6 nm in length within the columnar grains, and 70.8 ± 25.8 nm in width and 430.9 ± 155.4 nm in length within the relatively coarser region in the melt pool core) and the melt pool boundary region confirms that the PBF-LB Nd-Fe-B material can be classed as nanostructured. The dendrites, annotated in Fig. 4, are common in impure metals. This is because the pure crystals have a higher freezing point than the liquid with impurities and constitutional undercooling is a consequence [63]. During cooling down, the primary $Nd_2Fe_{14}B$ crystals grow faster (light grey features in the dark field TEM images), leaving the rest of the elements in the liquid to solidify at the boundaries of the dendrites, depicted as darker regions in the same images in Fig. 4(a), (c), and (e). Therefore, the boundaries of these grains and dendrites are Ti-rich across the melt pool and Zr-rich at the melt pool boundaries, as confirmed by the TEM-EDS maps in Fig. 3. Within the grains in the various regions of the melt pools, globular precipitates were observed (white features in the dark-field TEM images and black ones in the bright-field TEM images in Fig. 4) that according to the TEM-EDS maps in Fig. 3 were Nd-rich.

High-resolution TEM images of the nanocrystalline structure of this material are presented in Fig. 5. As evidenced by the diffraction contrast in the TEM bright field image in Fig. 5(a), the primary grains are crystalline. Fig. 5 (b–d) gives some lattice-resolved images of typical grain boundaries, in which the crystallite planes are annotated in yellow. The region filled between the primary grains appeared to be amorphous, as in Fig. 5 (b and d). This boundary region was found to be Ti-rich in TEM/EDS (Fig. 3) and is to be correlated with the APT findings.

The single atom maps collected using APT are presented in Fig. 6. The accurate compositions of the primary phase, interphase, and precipitates at the interphase were measured as displayed in Table 2. Thanks to the high resolution and accuracy of APT, the lack of Fe, Co, Nd, and Pr at the GBs was confirmed and the composition of the Nd-rich precipitates was confirmed to be $Nd_{15.7}Pr_{2.4}Zr_{3.0}Ti_{6.7}Co_{2.8}Fe_{53.5}B_{10.8}C_{1.7}$, which further supports the TEM analysis findings in Figs. 3–5. More interestingly, a small number of Nd-lean precipitates were detected in the interphase with a chemical composition of $Nd_{0.7}Pr_{0.1}Zr_{5.3}Ti_{9.4}Co_{2.5}Fe_{71.2}B_{10.4}C_{0.3}$, which is a Ti-B-Zr-rich iron-based precipitate. This evidence contradicts previous claims in the literature that speculate that the GB of this material is composed of α-Fe when processed by PBF-LB [26,47]. The APT analysis here confirmed that the interphase contains less Fe than the primary phase, which is in agreement with the TEM-EDS maps in Fig. 3. Combining the APT analysis with the TEM-EDS maps and the HR-TEM images, it can be asserted that the interphase between the primary phase in PBF-LB Nd-Fe-B magnets is an amorphous Ti-rich phase rather than α-Fe.

To summarise, the microstructure of PBF-LB Nd-Fe-B mainly consists of the $Nd_2Fe_{14}B$ phase, the amorphous Ti-B-Zr-rich iron-based phase at the interphase, in addition to a small amount of Ti-B-Zr-rich iron-based precipitates, and Nd-rich iron-based precipitates. The mechanisms of formation of this microstructure can be further understood through the microstructural observations in this section supported by the phase diagram of Nd-Fe-B [64]. Having the highest phase transition temperature compared to the other phases (B-rich: 1081 °C, α-Fe: 900 °C, and Nd-rich: 655 °C), $Nd_2Fe_{14}B$ (1180 °C) is the primary crystalline phase and it forms first during solidification consuming most of the Nd and Fe.

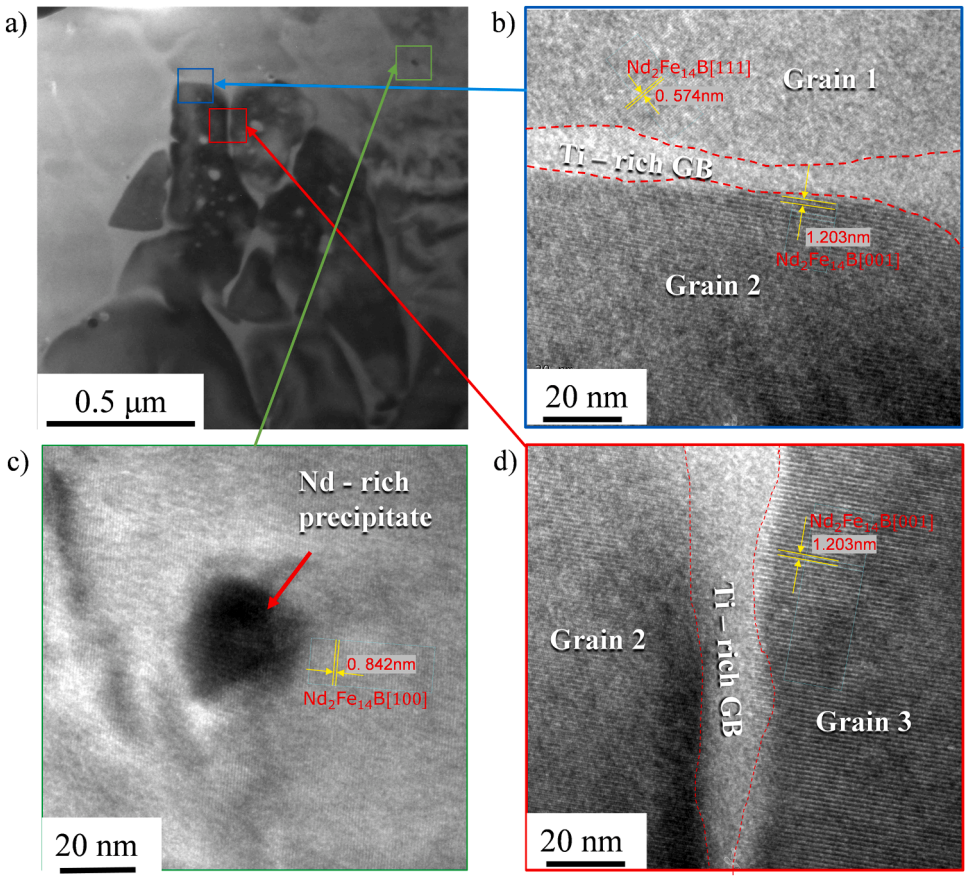

Fig. 5. (a) Conventional TEM showing the location of each HR-TEM image. (b) shows the interface between two grains with different crystal orientations. (c) shows an Nd-rich precipitate with the Nd Fe B matrix. (d) displays the interface between two grains with the same crystal orientation.

Compared to the chemical contents of 11.8 at% Nd and 82.4% at% Fe in the $Nd_2Fe_{14}B$ phase schematically, the composition of the MQP-S powder with only 7.5 at% Nd prohibits the formation of a continuous Nd-rich film at the interphase, hence, Nd-rich globular precipitates form at the interphase. The lower content of 75 at% Fe also prohibits the formation of the α-Fe phase. Primary grains with dendritic structures were formed in the as-printed material due to the presence of several elements, such as Pr, Zr, Co, and Cu. These additional elements can substitute some of the Nd and Fe in each $Nd_2Fe_{14}B$ unit cell to form the primary phase grains. The fraction of elements that are not consumed by the formation of $Nd_2Fe_{14}B$ remains at the GBs to form the amorphous Ti-B-Zr-rich iron-based phase and a small amount of the precipitates driven by the rapid solidification in the process.

The magnetic properties of a material are related to its microstructure. Therefore, it is common to tailor the morphology of the Nd-rich iron-based phase to be continuous and thin to enhance the magnetic properties of microcrystalline sintered Nd-Fe-B magnets [65–67]. A continuous non-magnetic Nd-rich phase acts as an insulator at the GBs inhibiting the nucleation of magnetic reversal between the primary $Nd_2Fe_{14}B$ grains [68]. The presence of an amorphous phase at the GBs in melt-spun nanocrystalline magnets was reported to function as an insulator between the $Nd_2Fe_{14}B$ grains enhancing the magnetic exchange coupling, similar to the function of the Nd-rich phase in sintered magnets [17]. In the PBF-LB Nd-Fe-B, although no continuous Nd-rich film was detected at the GBs, the amorphous GB phase can play the role of insulator [17]. However, the Nd-rich phase in the PBF-LB sample has much lower Nd content (measured to be 15.7 at% from APT) compared to the Nd-rich phase in the conventional sintered magnets, which is typically around 96 at% Nd, 3–5 at% Fe, and a trace of B. As a result, the insulating ability of the Nd-rich phase is questionable. On the other hand, the Nd-rich phase and Ti-B-Zr-rich iron-based precipitates can act as magnetic pores [69] and promote magnetic domain reversal between the primary grains and lower the coercivity.

3.2. Phase identification

Phase identification was conducted using TEM/selected area diffraction (SAD), XRD, and SEM/EBSD. The samples used in this study were 91± 0.5% dense [28]. SAD patterns were collected from the three regions of the melt pool. Typical TEM bright field images and the associated diffraction patterns are presented in Fig. 7. The $Nd_2Fe_{14}B$ phase was confirmed as the primary phase, as evidenced by the indexed SAD patterns matching the tetragonal $Nd_2Fe_{14}B$ (04–005–3154).

The XRD patterns of the loose powder and bulk samples are presented in Fig. 8. By matching the peaks on the XRD pattern of the MQP-S powder (Fig. 8(a)) with the PDF cards from the database (00–036–1296, 03–065–4899), most of the strong peaks distributed along the diffraction range 20–70° were identified to be the crystalline phase $Nd_2Fe_{14}B$. No significant crystallographic texture was observed from the XRD pattern. One of the peaks of $Nd_2Fe_{14}B$ and the α-Fe peak overlap at around 45° from the PDF cards (00–036–1296, 03–065–4899). The intense peak around 45° for $Nd_2Fe_{14}B$ and α-Fe indicates the existence of a significant amount of α-Fe in the powder. The XRD pattern of the powder agrees with the literature, according to the ternary Nd-Fe-B phase diagram [70]. The MQP-S powder with a nominal composition of $Nd_{7.5}Pr_{0.7}Zr_{2.6}Ti_{2.5}Co_{2.5}Fe_{75}B_{8.8}$ [48] is a RE-lean alloy since the content of the rare earth elements, including Nd and Pr, is 8.2 at%, which is significantly lower than the Nd content of 11.8 at% to form the $Nd_2Fe_{14}B$ phase stoichiometrically. Due to the excessive content of Fe, alloys with this composition mainly consist of $Nd_2Fe_{14}B$ and the additional α-Fe

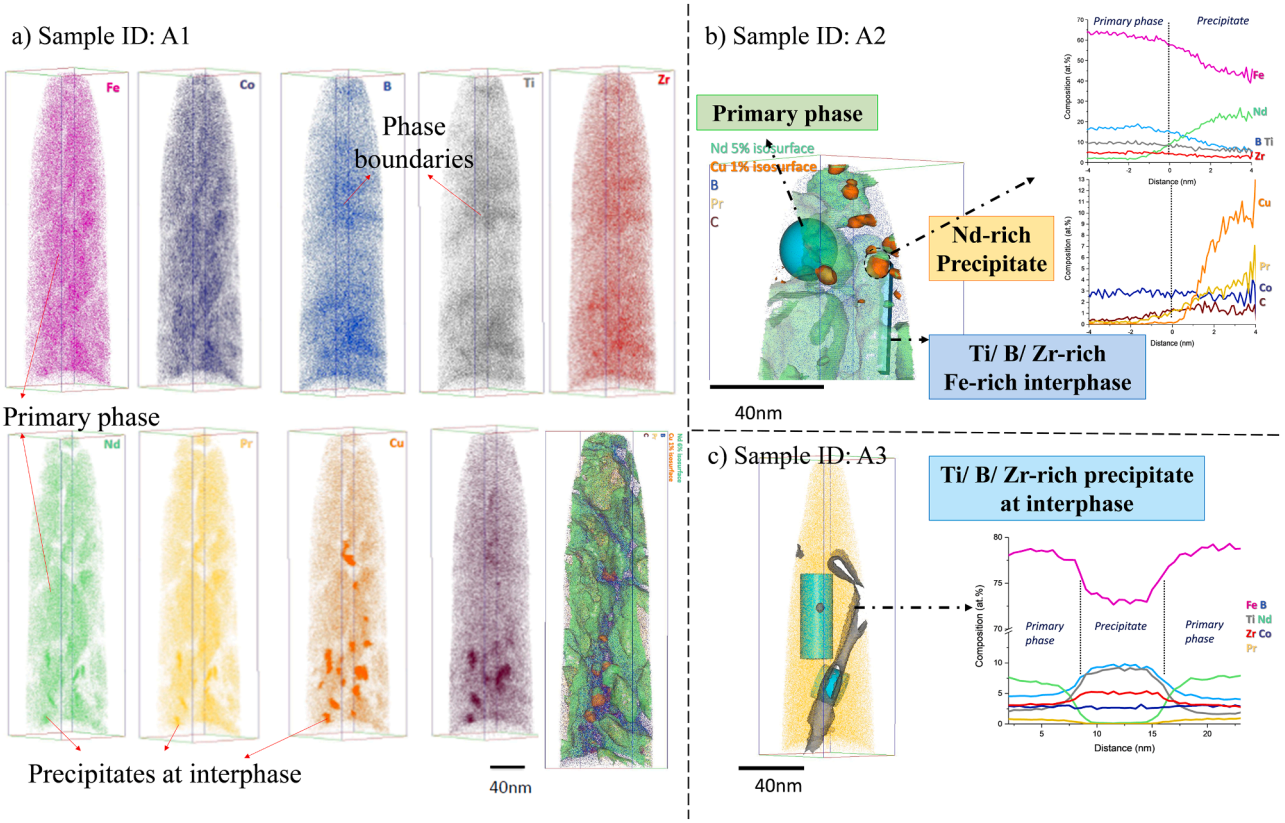

Fig. 6. (a) Single Atom maps for the elements detected in the APT experiment; (b) the composition of the primary phase, Ti-rich intergranular phase, Nd-rich and (c) Nd-lean precipitates at the interphase in the APT map.

Table 2
Chemical compositions from APT at the annotated regions in Fig. 6.

At% ID	Fe	B	Nd	Zr	Pr	Ti	Co	Cu	C
Primary phase	79.7	4.8	7.1	1.8	0.75	1.5	3.2	0.15	0.22
Interphase	64.7	15.4	0.96	5.1	0.11	10.7	2.6	0.02	0.28
Nd-rich precipitate	53.5	10.8	15.7	3.0	2.4	6.7	2.8	2.9	1.7
Ti/B/Zr-rich precipitate	71.2	10.4	0.67	5.3	0.07	9.4	2.54	0.03	0.28

* The APT-derived compositions of the phases in Table 2 total over 99%. Residual trace contamination elements including Si, P, Cr, and Mn make up the balance, but such minor peaks are near the detection limits, and were therefore omitted from further analysis.

phase.

As for the bulk sample (Fig. 8(b)), the intense peaks distributed over the diffraction range 20–70° were identified as the crystalline phase $Nd_2Fe_{14}B$ without significant crystallographic texture, similar to the powder. The main differences from the powder were the presence of a more amorphous background, a weaker peak around 45°, and unidentified weak peaks. The location of the amorphous peak matches best with the $Fe_5(CO)_{15}C$ Iron Carbonyl Carbide phase (PDF 01–076–1719) from the database, which indicates the amorphous phase is an iron-based amorphous phase. The amorphous background is attributed to the GB intergranular amorphous phase observed in HR-TEM (Fig. 5) and APT (Fig. 6). The peak around 45° for α-Fe and $Nd_2Fe_{14}B$ was much weaker than in the powder. The significant reduction in the intensity of the peak around 45° could be due to the suppression of the α-Fe phase formation by the rapid solidification of the melt pool during PBF-LB. However, since the α-Fe peak would overlap with one of the $Nd_2Fe_{14}B$ peaks at around 45°, the existence of α-Fe was hard to be distinguished from the XRD pattern. Neither α-Fe nor other crystalline phases were detected in the HRTEM study, and the chemical composition of the primary grains was fairly consistent in the APT study. Therefore, it is indicated that either the PBF-LB materials do not contain α-Fe, or the amount of α-Fe in the PBF-LB material is low and no α-Fe was consistent in the volumes sampled for HRTEM and APT in this study. The unidentified weak peaks can be associated with the small amounts of precipitated Nd-rich and Ti-B-Zr-rich iron-based phases in the nanocrystalline structure of the material, as observed in APT (Fig. 6). Since the higher intensity $Nd_2Fe_{14}B$ peaks were widely distributed along the range of the scanned diffraction angle range, they overshadowed the peaks corresponding to the small amounts of precipitates.

Three regions were selected for EBSD analysis, named EBSD areas i, ii and iii, annotated by the dashed boxes in Fig. 2(a) with the respective maps presented in Fig. 9. A variety of $RE_2M_{14}X$-type phases were analysed using AZtec. The lattice parameters of the $Pr_2Fe_{14}B$ phase were the best match to the EBSD patterns although the high Pr content in this phase did not match the EDS measurements (Table 1 and Fig. 6). The effects on the lattice parameter can be attributed to potential Pr, Zr, Cu, or Co substitutions of the Nd or Fe atoms [71–73].

The $Nd_2Fe_{14}B$ phase was the predominant phase in the three maps and no strong crystallographic texture was visible (i.e. the samples exhibited random crystalline orientations). This is in agreement with the HR-TEM and XRD findings (Figs. 5 and 8), indicating that the PBF-LB Nd-Fe-B magnet can be classed as an isotropic magnetic material.

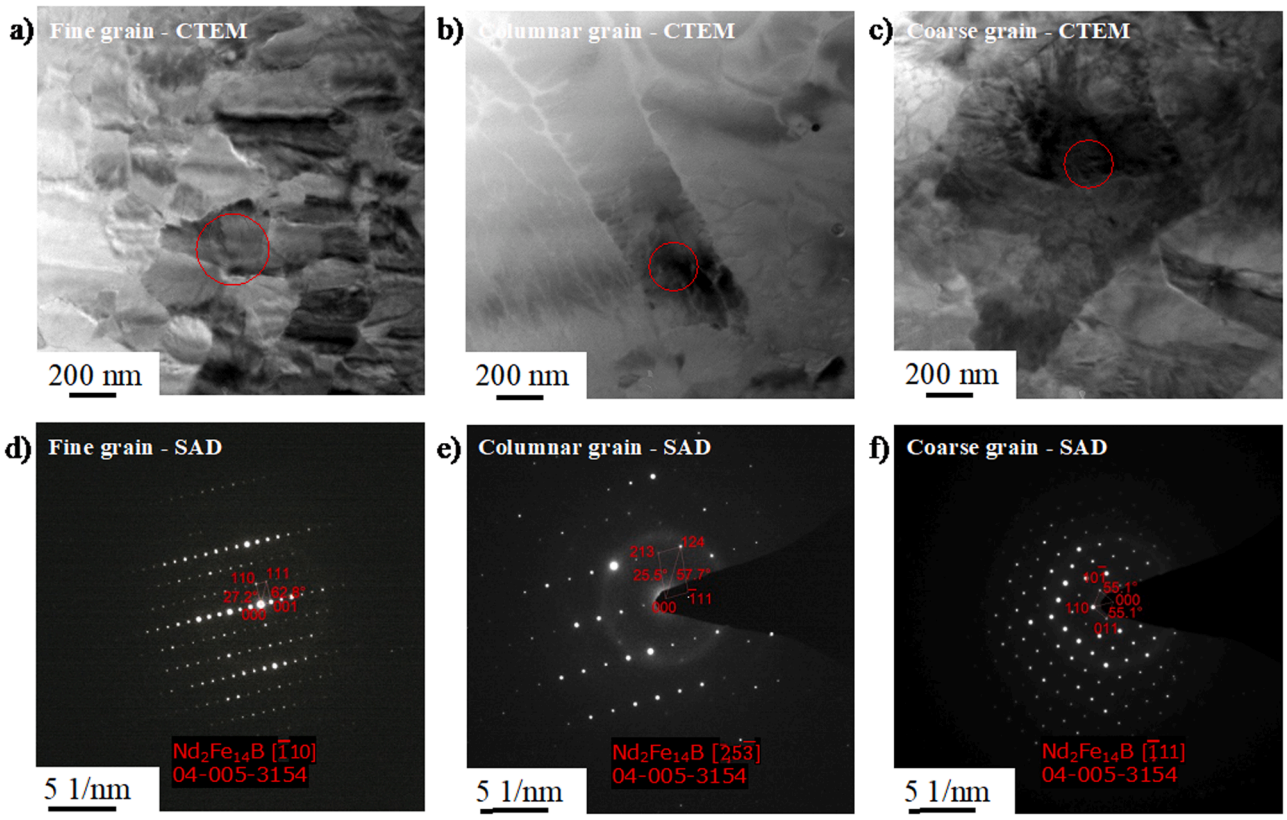

Fig. 7. Conventional TEM micrographs and Selected Area Diffraction patterns (SAD) from the coarse, columnar melt pool interface and fine-grained zones in (a,d), (b,e) and (c,f), respectively. All the patterns matched the tetragonal phase $Nd_2Fe_{14}B$ (04–005–3154).

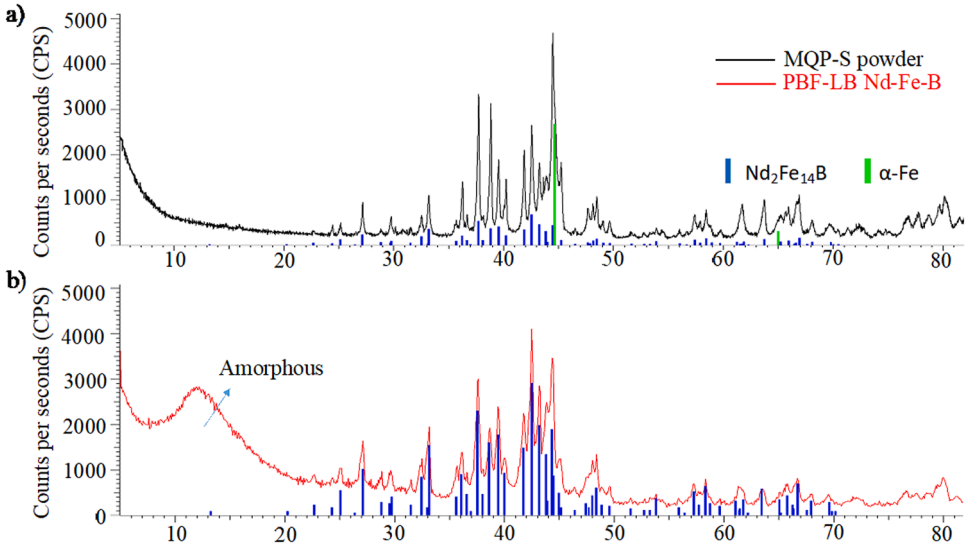

Fig. 8. XRD pattern showing the amorphous and crystalline phases of (a) the feedstock MQP-S powder and (b) the as-printed Nd-Fe-B sample. In both cases, the $Nd_2Fe_{14}B$ peaks are widely distributed along the diffraction range with higher intensity compared to the other precipitated phases. More α-Fe was detected in the powder feedstock and more amorphous phase was observed in the bulk sample.

The hierarchical grain structure observed in the electron microscope images was further supported by the EBSD maps. The map of the single track (Fig. 9(a)) and the top layer (Fig. 9(d)) support that the hierarchical grain structure with random crystalline alignment was formed during melt pool solidification rather than due to *in-situ* heat treatment. A random crystalline alignment of $Nd_2Fe_{14}B$ was evident in the maps of the single track, the top layer, and the mid layers of the sample. This random crystal alignment was caused by the preferential growth direction of the $Nd_2Fe_{14}B$ phase, namely [100] and [010] [33,74,75]. A hierarchical structure appeared in the single-track map (Fig. 9(a)). Due to the fact that there was no remelting or *in-situ* heat treatment applied and the single track was deposited on top of the sample, the hierarchical grain size distribution from top to bottom can be attributed to temperature gradient changes during the cooling process of the melt pool. The top layer and the middle layer maps also showed hierarchical grain structures. Repetitive melting and remelting cycles happen during the

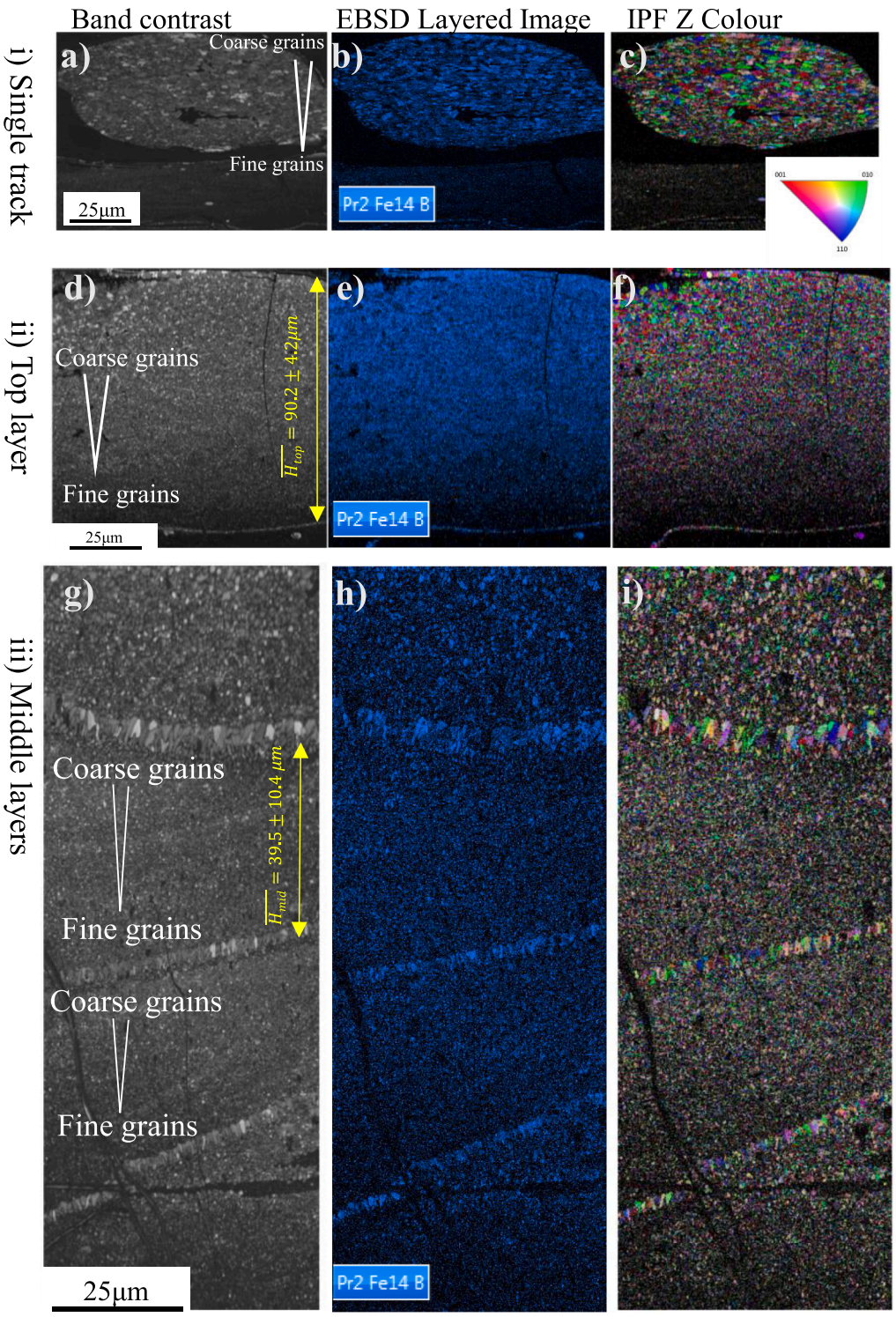

Fig. 9. EBSD map from the cross-section of the PBF-LB Nd-Fe-B sample. The band contract image, EBSD layered image of $Nd_2Fe_{14}B$ phase and the crystallographic texture of (a–c) the single track at the top of the sample; (d)–f) the top layer of a sample; and (h–j) middle layers of the sample, respectively. The nanocrystalline hierarchical grain structure of the melt pool along the build direction was observed in the band contract image (a, d and g). No significant crystallographic texture was observed in the samples (c, f and i), indicating the material has a preferred magnetization direction externally and is an isotropic magnet.

process of PBF-LB. The solidified layer in the middle of the part (Fig. 9 (c)) will be remelted when the next layer is deposited at the top and irradiated, except for the top layer (Fig. 9(b)). According to Fig. 9(d) and (g), the top layer has an average thickness of 90.2 ± 10.4 μm, while the mid-layers have an average thickness of 39.5 ± 4.2 μm. The top layer had only one melting and solidification cycle without remelting. The effect of remelting on the grain size distribution of the parts was studied by measuring the grain size from the band contrast maps of the top layer and the mid-layers. This is displayed in Fig. 10.

The equivalent circle diameters of the grains within the various regions of the top layer and the middle layers are plotted in Fig. 10 and the values are tabulated in Fig. 10(f). The grain size was measured down to 0.3 μm as a step size of 0.1 μm and a minimum number (3) of point per grain was used to define the minimum grain size. In general, the mean size of the grains in the middle layers D and E was finer than the top layer but similar to those at the bottom of the uppermost layer. Accordingly, the grains within layer E that were larger than 0.82 μm were re-melted during processing in the subsequent layer 'D' (Fig. 10 (d)). As with layer D, the grains larger than 1.2 μm are re-melted and re-solidified upon processing the following layer. Earlier studies showed

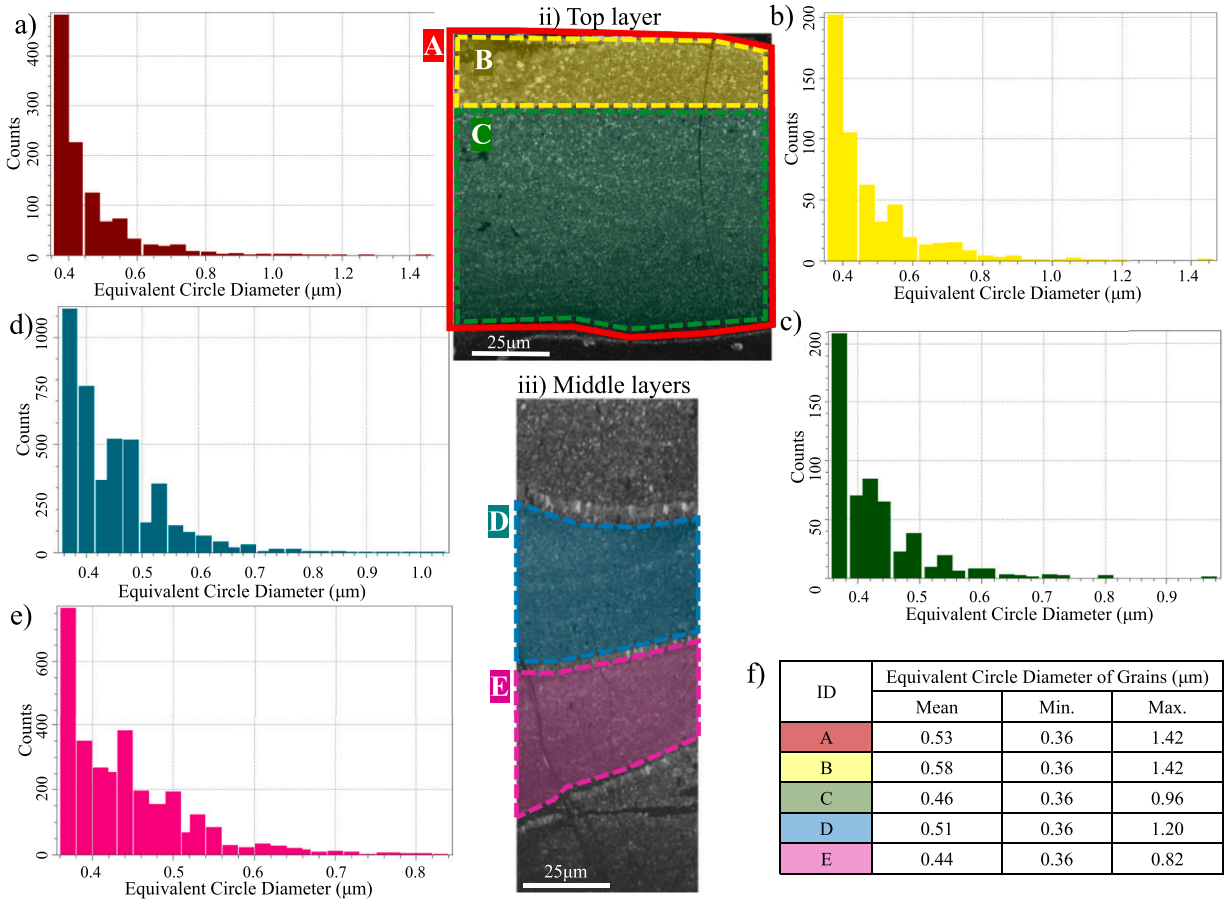

ID	Equivalent Circle Diameter of Grains (μm)		
	Mean	Min.	Max.
A	0.53	0.36	1.42
B	0.58	0.36	1.42
C	0.46	0.36	0.96
D	0.51	0.36	1.20
E	0.44	0.36	0.82

Fig. 10. The grain size distribution of the top layer and the mid layers of the PBF-LB Nd-Fe-B sample. Equivalent circle diameter of the grains (a) crossing the whole melt pool of the top layer; (b) the upper region of the top layer; (c) the lower region of the top layer; (d) and (e) the whole melt pool of the mid-layers. f) values of the grain size of the selected areas. The mean grain size of the mid-layer melt pools (D and E) was finer than the top layer, but comparable to the lower region of the top layer. This suggested that when another layer was deposited on the previous layer, the coarser grains at the upper region of layer (B) were re-melted and re-solidified into finer grains at the lower region of the following layer.

that the domain wall is positioned and pinned at the grain borders when the grain size is equivalent to the size of a single domain to enhance the resistance to demagnetization [76]. In coarse grains, the domains within each grain magnetically couple with each other and reduce resistance to demagnetisation. It can be concluded that partial remelting of portions of each layer in additive manufacturing using PBF-LB can facilitate the

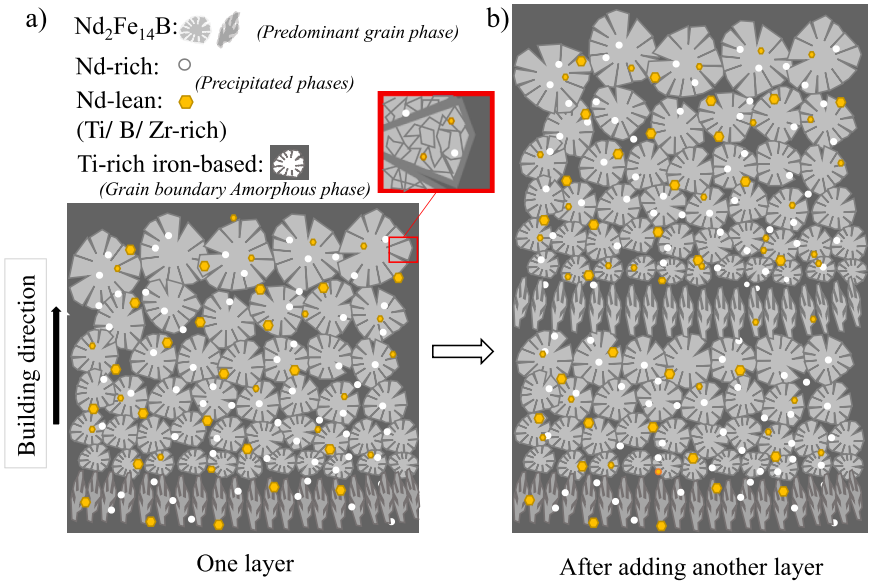

Fig. 11. Schematic illustration of the microstructure of the PBF-LB Nd-Fe-B. The material mainly consisted of a crystalline phase and an amorphous intergranular phase. The morphology of the crystalline phase grains is polygonal in the melt pool area, columnar at the melt pool boundaries and globular at the intergranular phase precipitates. The polygonal grains change from coarse to fine from the top to bottom of the melt pool due to the cooling gradient. The polygonal and columnar grains were mainly $Nd_2Fe_{14}B$ phase. Zr was precipitated at the grain boundaries of the columnar grains and the polygonal grains in the HAZ of the melt pool.

transformation of the coarser grains into finer ones, which is favourable for better permanent magnetic properties.

3.3. Relationship between the PBF-LB microstructure and the magnetic performance

A schematic illustration is presented in Fig. 11 that describes the scenario of the formation of the Nd-Fe-B microstructure during layer-by-layer manufacturing using PBF-LB based on integrating the findings from the various techniques used in this study. The printed material is composed of primary $Nd_2Fe_{14}B$ surrounded by amorphous intergranular Ti-rich iron-based GBs, in addition to small amounts of Nd-rich (globular) and Nd-lean (Ti-B-Zr-rich) iron-based precipitates. Atomic substitutions of Nd and Fe by the additional elements in the feedstock powder (Pr, Zr, Ti, Co, Cu, and C) occur, affecting the actual lattice parameters, which misled the XRD and EDS analyses, as confirmed by EBSD.

When the first layer of powder was irradiated by the laser beam, as shown in Fig. 11(a), polygonal grains formed within the melt pool and columnar grains at the melt pool boundaries due to the chemical composition ($Nd_{7.5}Pr_{0.7}Zr_{2.6}Ti_{2.5}Co_{2.5}Fe_{75}B_{88}$) of the MQP-S powder and the rapid cooling rates in PBF-LB. After depositing and irradiating the following layer of powder, as shown in Fig. 11(b), the new powder layer is melted, partially remelting the previously solidified layer. Similar to the proceeding layer, columnar grains as well as randomly orientated polygonal ones with a gradient change in size form. According to the EBSD map of the single track, the polygonal grains within the melt pool core were relatively coarser in the upper than the lower section.

The magnetic properties of the as-printed samples tested at temperatures varying between 20 and 200°C are displayed in Fig. 12. The temperature coefficients of the intrinsic coercivity α and remanence β were calculated from the results measured at room temperature (20 °C) and 150 °C. The properties of conventional sintered magnets, rare-earth-element-lean powder MQP-S, dense Spark plasma sintered (SPS) samples produced from gas-atomized MQP-S powder, and melt-spun MQU-F flakes, which have a higher content of the rare-earth element, are presented in Table 3 for comparison. The magnetic properties, including the intrinsic coercivity, remanence, and energy product, of the conventional anisotropic sintered magnets were significantly higher than the others owing to their anisotropy. On one hand, the magnetic properties of the

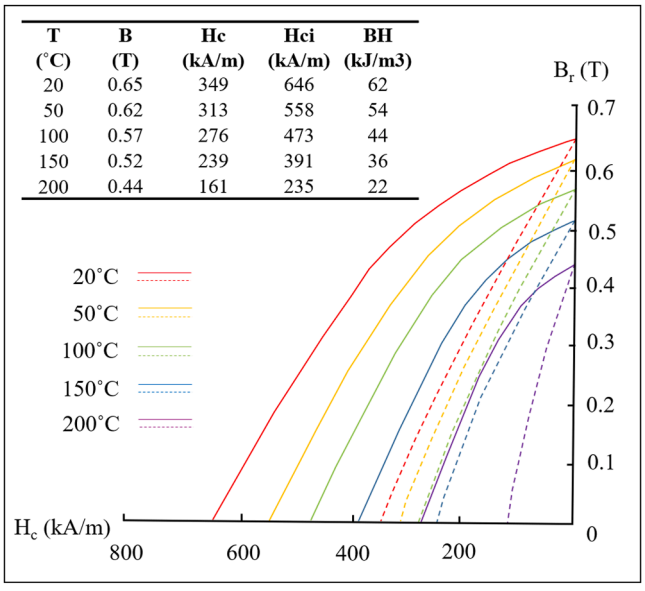

Fig. 12. Demagnetization curves of as-printed magnets at varying temperatures after magnetisation.

Table 3
Magnetic properties and calculated temperature coefficients of remanence and intrinsic coercivity of samples including powder and bulk samples prepared by a range of methods.

	Anisotropy	B_r (T)	H_{ci} (kA/m)	$(BH)_{max}$ (kJ/m^3)	Relative density	Powder composition	α (%/ °C)	β (%/ °C)	Temperature interval	Refs.
Hot-deformed	Anisotropic	1.22	1600	–	–	$Nd_{14.2}Fe_{75.62}Co_{3.81}Ga_{0.71}B_{5.66}$	−0.10	−0.38	20–180 °C	[78]
Sintered		1.12	2336	245	99.9%	$Nd_{22.5}Dy_{10}Fe_{65.4}$ $Cu_{0.15}Al_{0.4}Ga_{0.15}Nb_{0.4}B$	−0.09	−0.39	20–150 °C	[79]
Sintered		1.33	1480	356	99.9%	$Nd_{28.25}Dy_{2.75}Fe_{67.67}Al_{0.15}Ga_{0.1}Nb_{0.1}B_{0.98}$	–	–		[16]
Sintered	Isotropic	0.53	1416	42	99.9%	$Nd_{28.25}Dy_{2.75}Fe_{67.67}Al_{0.15}Ga_{0.1}Nb_{0.1}B_{0.98}$	–	–		
SPS		0.82	1665	123	99.9%	$Nd_{13.6}Fe_{73.6}Co_{6.6}Ga_{0.6}B_{5.6}$ (MQU-F)	−0.09	−0.45	20–120 °C	[77]
SPS		0.54	615	37	77%	$Nd_{7.5}Pr_{0.7}Zr_{2.6}Ti_{2.5}Co_{2.5}Fe_{75}B_{8.8}$ (MQP-S)	−0.12	−0.39		
MQP-S powder		0.73–0.76	670–705	80–92	–		−0.13	−0.40	20–100 °C	[32]
PBF-LB		0.63	921	63	–		–	–	–	[33]
PBF-LB		0.65	603	62	91%		−0.15	−0.30	20–150 °C	This work

*As per the powder supplier, the MQP-S powder's magnetic characteristics were measured using a vibrating sample magnetometer. The corresponding sample consists of a plastic pill where the powder is pressed into and sealed. However, the density was not provided by the supplier, so the properties of the powder in the datasheet were assumed to have been balanced and to have a full density. The other materials for comparison were not fully dense and the relative density is presented in the table.

PBF-LB samples in this study were lower than the MQP-S powder due to the relatively higher porosity content (9%) [28]. On the other hand, the area enclosed by the demagnetisation curve in the second quadrant (Fig. 12) is smaller than that of the feedstock material [32], indicating that the PBF-LB Nd-Fe-B is magnetically 'softer' than the powder. This may be due to the relatively lower density of the permanent magnetic phase and the existence of the Nd-rich and Nd-lean precipitates and amorphous GBs. Bittner et al. improved the magnetic properties of PBF-LB parts through careful parameter optimisation and achieved the magnetic properties of remanence of 0.63 T, coercivity of 921 kA/m and maximum energy product of 63 kJ/m^3, exceeding previously published works' values significantly [33]. Although the coercivity of the samples in the current study was relatively lower compared to the ones published by Bittner et al., the remanence and energy product were comparable. Meanwhile, the microstructural results from SEM (Fig. 2), show the size and morphology of the grains to be similar in this manuscript and the work of Bittner et al. [33]. The focus of our manuscript though is on the in-depth understanding of the microstructure of PBF-LB Nd-Fe-B and how it correlates to the performance of the material. However, the properties reported in this study were superior to the SPS counterpart owing to the nanocrystalline structure of the PBF-LB samples confirmed in this study [28] and the suppressed α-Fe phase [26,28,77]. The higher properties of samples produced from MQU-F flakes are attributed to the excessive RE content, which enhances the resistance to demagnetization. It can be observed that the temperature had a strong influence on the PBF-LB Nd-Fe-B magnets (Fig. 12) as with other magnets [32, 77–79]. Compared to other types of permanent magnets, the high energy product of the Nd-Fe-B magnets offers the potential advantage of lighter weight in applications such as the permanent magnet synchronous motors [2], though the curie temperature is lower, which limits its application temperature [80]. As the temperature rises above room temperature, the intrinsic coercivity and remanence decrease, which makes the magnets more vulnerable to demagnetization and more electric current at a constant torque would be needed. Consequently, it is important to investigate the temperature dependence of the magnetic properties of a permanent magnet. The magnetic properties, remanence, coercivity, and energy products deteriorated with an increase in the demagnetising temperature. Negative values of α and β indicate a decrease in remanence and coercivity of a magnet with increasing temperature. The value of β (−0.30%/ °C) of the as-printed sample was higher than the unprocessed MQP-S powder, the RE-lean MQP-S SPS magnet, RE-rich MQU-F SPS magnets, RE-rich conventional sintered, and hot-deformed magnets. The higher value indicates the as-printed sample was less susceptible to demagnetization as a function of increasing the temperature compared to the other magnets. The value of α (−0.15%/ °C) was comparable to the state-of-the-art. As a result, higher residual magnetic properties of PBF-LB Nd-Fe-B magnets for higher-temperature applications are expected by improving the coercivity at room temperature.

Following this comprehensive study, the structure-property relationship can be elucidated by correlating the results from the microstructure investigations with the permanent magnetic tests. The PBF-LB Nd-Fe-B magnet is isotropic (EBSD maps and HR-TEM images), consisting of nanocrystalline grains with random crystalline alignment. The permanent (hard) magnetic property can be mainly attributed to the primary $Nd_2Fe_{14}B$ phase. The morphology of the $Nd_2Fe_{14}B$ grains was polygonal with a hierarchical grain structure along the depth of the melt pool (Fig. 2). From the in-depth microstructure study on the magnet using MQP-S powder consisting of limited Nd, Fe, and B elements besides the additional elements (Pr, Zr, Ti, Co, Cu and C), the GB phase was confirmed not to be the soft magnetic α-Fe phase. There is no continuous Nd-rich phase at the GBs of the $Nd_2Fe_{14}B$ grains to insulate and inhibit magnetic domain reversal between the grains (Figs. 3 and 6), instead, there is an amorphous Ti-rich phase with small amounts of intergranular Nd-rich and Nd-lean precipitates. The magnetic insulation ability of the Ti-rich iron-based phase observed at the GBs and the effect of the intergranular precipitates on the magnetic properties require further investigation in the future. Owing to the rapid cooling process, the PBF-LB process has been shown to be a promising AM method for the production of net-shape magnets with nanocrystalline microstructure. Although columnar grains forming at the melt pool boundaries have a negative impact on the coercivity, considering the effect of aspect ratio, the maximum grain size of the columnar grains and the polygonal grains within the melt pool and the nanostructured microstructure are preferable for higher permanent magnetic properties. Additionally, the effect of grain refinement during remelting can be potentially applied to modify the microstructure to enhance the magnetic properties.

4. Conclusion

In this study, Nd-Fe-B powder was processed by PBF-LB AM to produce magnets that were analysed in depth for their metallurgical and magnetic properties. Based on the findings of this study, the following conclusions can be drawn:

1. The printed magnet is composed of isotropic amorphous-crystalline nanocomposite material.
2. When processed by PBF-LB, the Nd-lean feedstock material resulted in a microstructure that consists of the primary $Nd_2Fe_{14}B$ phase, amorphous Ti-rich iron-based grain boundaries, in addition to Nd-rich and Nd-lean iron-based precipitates in the matrix of the amorphous Ti-rich iron-based GB intergranular phase.
3. The primary $Nd_2Fe_{14}B$ grains with polygonal morphology and random crystalline alignment are distributed hierarchically in size across the melt pools. The grains at the melt pool boundaries are columnar.
4. When the pre-solidified layer was partially remelted while processing the subsequent layer, the coarse grains were re-melted and re-solidified into finer grains, favourable for the permanent magnetic properties.
5. The temperature coefficients of these PBF-LB magnets were comparable to most common magnets. The potential use of PBF-LB in high-temperature applications will require further coercivity enhancement at room temperature through optimisations of the chemical composition of the feedstock powder and process parameters.

Declaration of Competing Interest

The authors declare that they have no known competing financial interests or personal relationships that could have appeared to influence the work reported in this paper.

Acknowledgments

Julan Wu gratefully acknowledges the support of the Centre for Additive Manufacturing (CfAM, University of Nottingham) and funding provided by the INNOVATIVE doctoral programme. The INNOVATIVE programme is partially funded by the Marie Curie Initial Training Networks (ITN) action (project number 665468) and partially by the Institute for Aerospace Technology (IAT) at the University of Nottingham. We also wish to acknowledge the support of Henry Royce Institute for advanced materials through the Student Access Scheme (EPSRC Grant Number EP/R00661X/1) enabling access to atom probe tomography facilities at the University of Oxford; and Mr Mark Hardy from the Centre for Additive Manufacturing (CfAM, University of Nottingham, UK), Mr Nigel Neate and Dr Christopher Parmenter from Nanoscale and Microscale Research Centre (nmRC, University of Nottingham, UK) for their support with samples preparation and testing.

References

[1] D. Brown, B.M.M. Ma, Z. Chen, Developments in the processing and properties of NdFeb-type permanent magnets, J. Magn. Magn. Mater. 248 (2002) 432–440, https://doi.org/10.1016/S0304-8853(02)00334-7.

[2] S. Tumanski, Modern magnetic materials - The review, Prz. Elektrotechniczny. 86 (2010) 1–15.

[3] D.P. Arnold, Review of microscale magnetic power generation, IEEE Trans. Magn. 43 (2007) 3940–3951, https://doi.org/10.1109/TMAG.2007.906150.

[4] Y. Luo, 25 years development of NdFeB magnet industry, in: 20th Inernational Work. Rare Earth Perm. Magn. Their Appplications, Knossos, Crete, 2008: pp. 27–36.

[5] T. Saito, T. Takeuchi, H. Kageyama, Magnetic properties of Nd–Fe–Co–Ga–B magnets produced by spark plasma sintering method, J. Appl. Phys. 97 (2005) 10H103, https://doi.org/10.1063/1.1849693.

[6] S. Hu, J. Liu, Y. Liu, J. Zhang, H. Yu, K. Su, Y. Huang, Z. Liu, Enhancing the properties of spark plasma sintered nanocrystalline NdFeB magnets by the addition of Cu-Zn alloy and Dy2O3 powders, J. Electron. Mater. 49 (2020) 720–727, https://doi.org/10.1007/s11664-019-07703-8.

[7] Z. Samard, L. Scherf, R. Kessler, S. Kobe, Ž. Kristina, A spark-plasma-sintering approach to the manufacture of anisotropic Nd-Fe- B permanent magnets, J. Magn. Magn. Mater. 502 (2020), https://doi.org/10.1016/j.jmmm.2020.166504.

[8] L. Leich, A. Röttger, R. Kuchenbecker, W. Theisen, Electro-discharge sintering of nanocrystalline NdFeB magnets: process parameters, microstructure, and the resulting magnetic properties, J. Mater. Sci. Mater. Electron. 31 (2020) 20431–20443, https://doi.org/10.1007/s10854-020-04562-6.

[9] E. Cannella, C.V. Nielsen, N. Bay, Resistance sintering of NdFeBCo permanent magnets and analysis of their properties, CIRP J. Manuf. Sci. Technol. 29 (2020) 88–98, https://doi.org/10.1016/j.cirpj.2020.02.005.

[10] E. Castle, R. Sheridan, W. Zhou, S. Grasso, A. Walton, M.J. Reece, High coercivity, anisotropic, heavy rare earth-free Nd-Fe-B by Flash Spark Plasma Sintering, Sci. Rep. 7 (2017) 11134, https://doi.org/10.1038/s41598-017-11660-9.

[11] Q.F. Zhou, S.Z. Dong, Super Permanent Magnet: Rare Earth Iron Series Permanent Magnet, 2nd Ed., Metallurgical Industry Press, Beijing, China, 2004.

[12] M. Sagawa, S. Fujimura, N. Togawa, H. Yamamoto, Y. Matsuura, New material for permanent magnets on a base of Nd and Fe (invited), J. Appl. Phys. 55 (1984) 2083–2087, https://doi.org/10.1063/1.333572.

[13] K. Hono, H. Sepehri-Amin, Strategy for high-coercivity Nd–Fe–B magnets, Scr. Mater. 67 (2012) 530–535, https://doi.org/10.1016/J.SCRIPTAMAT.2012.06.038.

[14] T.S. Chin, M.P. Hung, D.S. Tsai, K.F. Wu, W.C. Chang, Compaction and sintering behaviors of a Nd-Fe-B permanent magnet alloy, J. Appl. Phys. 64 (1988) 5531–5533, https://doi.org/10.1063/1.342326.

[15] X. Liu, T. Ma, X. Wang, M. Yan, Coercivity enhancement of low rare earth Nd–Fe–B sintered magnets by optimizing microstructure, J. Magn. Magn. Mater. 382 (2015) 26–30, https://doi.org/10.1016/J.JMMM.2015.01.043.

[16] X.G. Cui, C.Y. Cui, X.N. Cheng, X.J. Xu, T.Y. Ma, M. Yan, C. Wang, Effects of alignment on the magnetic and mechanical properties of sintered Nd-Fe-B magnets, J. Alloys Compd. 563 (2013) 161–164, https://doi.org/10.1016/j.jallcom.2013.02.093.

[17] S. Li, B. Gu, H. Bi, Z. Tian, G. Xie, Y. Zhu, Y. Du, Role of amorphous grain boundaries in nanocomposite NdFeB permanent magnets, J. Appl. Phys. 92 (2002) 7514–7518, https://doi.org/10.1063/1.1524311.

[18] J. Ormerod, S. Constantinides, Bonded permanent magnets: current status and future opportunities (invited), J. Appl. Phys. 81 (1997) 4816–4820, https://doi.org/10.1063/1.365471.

[19] W.Q. Liu, R.J. Hu, M. Yue, Y.X. Yin, D.T. Zhang, Preparation and properties of isotropic Nd-Fe-B bonded magnets with sodium silicate binder, J. Magn. Magn. Mater. 435 (2017) 187–193, https://doi.org/10.1016/J.JMMM.2017.04.009.

[20] M.P. Paranthaman, N. Sridharan, F.A. List, S.S. Babu, R.R. Dehoff, S. Constantinides, Additive Manufacturing of Near-net Shaped Permanent Magnets, Oak Ridge National Laboratory, Oak Ridge, TN, USA, 2016, https://doi.org/10.2172/1311265.

[21] M.G. Garrell, B. Ma, A.J. Shih, E. Lara-curzio, R.O. Scattergood, Mechanical properties of polyphenylene-sulfide (PPS) bonded Nd-Fe-B permanent magnets, Mater. Sci. Eng. A 359 (2003) 375–383, https://doi.org/10.1016/S0921-5093(03)00400-3.

[22] L. Li, A. Tirado, I.C. Nlebedim, O. Rios, B. Post, V. Kunc, R.R. Lowden, E. Lara-Curzio, R. Fredette, J. Ormerod, T.A. Lograsso, M.P. Paranthaman, Big Area Additive Manufacturing of High Performance Bonded NdFeB Magnets, Sci. Rep. 6 (2016) 1–7, https://doi.org/10.1038/srep36212.

[23] M.P. Paranthaman, C.S. Shafer, A.M. Elliott, D.H. Siddel, M.A. McGuire, R. M. Springfield, J. Martin, R. Fredette, J. Ormerod, Binder jetting: a novel ndfeb bonded magnet fabrication process, Jom 68 (2016) 1978–1982, https://doi.org/10.1007/s11837-016-1883-4.

[24] M.P. XParanthaman, I.C. Nlebedim, F. Johnson, S.K. Mccall, O. Ridge, Additive manufacturing of permanent magnets, Mater. Matters 11 (2016) 1–8.

[25] T. Kolb, F. Huber, B. Akbulut, C. Donocik, N. Urban, D. Maurer, J. Franke, Laser beam melting of NdFeB for the production of rare-earth magnets, in: Proceedings of the 6th International Electric Drives Production Conference (EDPC), 2016, pp. 34–40, https://doi.org/10.1109/EDPC.2016.7851311.

[26] J. Jaćimović, F. Binda, L.G. Herrmann, F. Greuter, J. Genta, M. Calvo, T. Tomše, R. A. Simon, Net shape 3D printed NdFeB permanent magnet, Adv. Eng. Mater. 19 (2017) 19, https://doi.org/10.1002/adem.201700098. No.8, 1700098.

[27] F. Bittner, J. Thielsch, W.G. Drossel, Laser powder bed fusion of Nd–Fe–B permanent magnets, Prog. Addit. Manuf. (2020), https://doi.org/10.1007/s40964-020-00117-7.

[28] J. Wu, N.T. Aboulkhair, M. Degano, I. Ashcroft, R.J.M.M. Hague, Process-structure-property relationships in laser powder bed fusion of permanent magnetic Nd-Fe-B, Mater. Des. 209 (2021), 109992, https://doi.org/10.1016/J.MATDES.2021.109992.

[29] C. Huber, G. Mitteramskogler, M. Goertler, I. Teliban, M. Groenefeld, D. Suess, Additive manufactured isotropic NdFeB magnets by stereolithography, fused filament fabrication, and selective laser sintering, Materials (Basel) 13 (2019), https://doi.org/10.3390/ma13081916.

[30] C. Huber, H. Sepehri-Amin, M. Goertler, M. Groenefeld, I. Teliban, K. Hono, D. Suess, Coercivity enhancement of selective laser sintered NdFeB magnets by grain boundary infiltration, Acta Mater. 3 (2019) 2–6, https://doi.org/10.1016/J.ACTAMAT.2019.04.037.

[31] B.M. Ma, J.W. Herchenroeder, B. Smith, M. Suda, D.N. Brown, Z. Chen, Recent development in bonded NdFeB magnets, J. Magn. Magn. Mater. 239 (2002) 418–423, https://doi.org/10.1016/S0304-8853(01)00609-6.

[32] Magnequench, MQP-S-11-9-20001 powder data sheet, (2020) 1–2. https://070.pdf.com/wp-content/uploads/2017/09/mqp-s-11-9-20001- (accessed August 4, 2023).

[33] F. Bittner, J. Thielsch, W. Drossel, Microstructure and magnetic properties of Nd-Fe-B permanent magnets produced by laser powder b e d fusion, Scr. Mater. 201 (2021), 113921, https://doi.org/10.1016/j.scriptamat.2021.113921.

[34] J.F. Herbst, R2Fe14B materials: intrinsic properties and technological aspects, Rev. Mod. Phys. 63 (1991) 819–898, https://doi.org/10.1103/RevModPhys.63.819.

[35] S. Bance, B. Seebacher, T. Schrefl, L. Exl, M. Winklhofer, G. Hrkac, G. Zimanyi, T. Shoji, M. Yano, N. Sakuma, M. Ito, A. Kato, A. Manabe, Grain-size dependent demagnetizing factors in permanent magnets, J. Appl. Phys. 116 (2014) 1–18, https://doi.org/10.1063/1.4904854.

[36] K. Hono, H. Sepehri-Amin, Strategy for high-coercivity Nd-Fe-B magnets, Scr. Mater. 67 (2012) 530–535, https://doi.org/10.1016/j.scriptamat.2012.06.038.

[37] A. El-Moneim, A. Gebert, F. Schneider, O. Gutfleisch, L. Schultz, Grain growth effects on the corrosion behavior of nanocrystalline NdFeB magnets, Corros. Sci. 44 (2002) 1097–1112, https://doi.org/10.1016/S0010-938X(01)00123-8.

[38] J. Lam, P. Katti, M. Biete, M. Mungai, S. Ashshareef, K. Neikirk, E.G. Lopez, Z. Vue, T.A. Christensen, H.K. Beasley, T.A. Rodman, S.A. Murray, J.L. Salisbury, B. Glancy, J. Shao, R.O. Pereira, E.D. Abel. A Universal Approach to Analyzing Transmission Electron Microscopy with ImageJ, 2021. https://doi.org/10.3390/cells10092177.

[39] K.V. Yang, Y. Shi, F. Palm, X. Wu, P. Rometsch, Materialia columnar to equiaxed transition in Al-Mg (-*Sc*) -Zr alloys produced by selective laser melting, Scr. Mater. 145 (2018) 113–117, https://doi.org/10.1016/j.scriptamat.2017.10.021.

[40] M. Simonelli, Microstructure Evolution and Mechanical Properties of Selective Laser Melted Ti-6Al-4V, University of Loughborough, 2014.

[41] N.T. Aboulkhair, I. Maskery, C. Tuck, I. Ashcroft, N.M. Everitt, The microstructure and mechanical properties of selectively laser melted AlSi10Mg: the effect of a conventional T6-like heat treatment, Mater. Sci. Eng. A 667 (2016) 139–146, https://doi.org/10.1016/j.msea.2016.04.092.

[42] K.V. Yang, Y. Shi, F. Palm, X. Wu, P. Rometsch, Columnar to equiaxed transition in Al-Mg(-*Sc*)-Zr alloys produced by selective laser melting, Scr. Mater. 145 (2018) 113–117, https://doi.org/10.1016/j.scriptamat.2017.10.021.

[43] H. Zhang, Y. Pan, Y. He, Effects of annealing on the microstructure and properties of 6FeNiCoCrAlTiSi high-entropy alloy coating prepared by laser cladding, J. Therm. Spray Technol. 20 (2011) 1049–1055, https://doi.org/10.1007/s11666-011-9626-0.

[44] J.D. Livingston, Magnetic domains in sintered Fe-Nd-B magnets, J. Appl. Phys. 57 (1985) 4137–4139, https://doi.org/10.1063/1.334644.

[45] H. Sepehri-Amin, T. Ohkubo, K. Hono, Micromagnetic simulations of magnetization reversals in Nd-Fe-B based permanent magnets, Mater. Trans. 57 (2016) 1221–1229, https://doi.org/10.2320/matertrans.M2015457.

[46] M. Skalon, M. Görtler, B. Meier, S. Arneitz, N. Urban, S. Mitsche, C. Huber, J. Franke, C. Sommitsch, Influence of melt-pool stability in 3D printing of ndfeb magnets on density and magnetic properties, Materials 13 (2020), https://doi.org/10.3390/ma13010139 (Basel).

[47] D. Goll, F. Trauter, T. Bernthaler, J. Schanz, H. Riegel, G. Schneider, Additive Manufacturing of Bulk Nanocrystalline FeNdB Based Permanent Magnets, Micromachines 12 (2021), https://doi.org/10.3390/mi12050538 (Basel).

[48] MQP-S-11-9 Material safety data sheet, Magnequech (2016). https://mqitechnology.com/product/mqp-s-11-9-20001/.

[49] I. Betancourt, H.A. Davies, Influence of Zr and Nb dopant additions on the microstructure and magnetic properties of nanocomposite RE2(Fe,Co)14B/α(Fe, Co) (RE = Nd-Pr) alloys, J. Magn. Magn. Mater. 261 (2003) 328–336, https://doi.org/10.1016/S0304-8853(02)00366-9.

[50] A. Shaaban, Effects of Zr Substitution in NdFeB Permanent Magnets, AIP Conf. Proc. 909 (2007) 63–67, https://doi.org/10.1063/1.2739826.

[51] C. Kuo, The Effect of Zr and ZrB 2 additions to NdFeB alloys, University of Birmingham (2010). https://etheses.bham.ac.uk/id/eprint/1018/.

[52] N. Henry, K. Lonsdale, Internaltional Tables for X-ray Crystallography, Kynoch Press, Birmingham, 1952.

[53] D.J. Branagan, R.W. McCallum, Altering the cooling rate dependence of phase formation during rapid solidification in the Nd2Fe14B system, J. Magn. Magn. Mater. 146 (1995) 89–102, https://doi.org/10.1016/0304-8853(94)01646-1.

[54] Z. Chen, B.R. Smith, D.N. Brown, B.M. Ma, Effect of Zr substitution for rare earth on microstructure and magnetic properties of melt-spun (Nd 0.75Pr 0.25) 12.5-xZr xFe 82B 5.5 (x=0-3) ribbons, J. Appl. Phys. 91 (2002) 8168–8170, https://doi.org/10.1063/1.1446119.

[55] J.P. Kruth, L. Froyen, J. Van Vaerenbergh, P. Mercelis, M. Rombouts, B. Lauwers, Selective laser melting of iron-based powder, J. Mater. Process. Technol. 149 (2004) 616–622, https://doi.org/10.1016/J.JMATPROTEC.2003.11.051.
[56] S. Gorsse, C. Hutchinson, M. Gouné, R. Banerjee, Additive manufacturing of metals: a brief review of the characteristic microstructures and properties of steels, Ti-6Al-4V and high-entropy alloys, Sci. Technol. Adv. Mater. 18 (2017) 584–610, https://doi.org/10.1080/14686996.2017.1361305.
[57] A.G. Savchenko, T.M. Medvedeva, I.V. Shchetinin, V.P. Menushenkov, M. V. Gorshenkov, E.S. Savchenko, I.G. Bordyuzhin, Phase-structural state diagrams and hysteresis properties of rapidly solidified alloy Nd10.4Zr4.0Fe75.1Co4.1B6.4 after heat treatment, J. Alloys Compd. 707 (2017) 205–209, https://doi.org/10.1016/j.jallcom.2017.01.002.
[58] Z. Tian, S. Li, K. Peng, B. Gu, J. Zhang, M. Lu, Y. Du, The microstructure and magnetic properties of NdFeB magnets directly solidified at a low cooling rate, Mater. Sci. Eng. A 380 (2004) 143–146, https://doi.org/10.1016/j.msea.2004.03.077.
[59] Z. Chen, H. Okumura, G.C. Hadjipanayis, Q. Chen, Microstructure refinement and magnetic property enhancement of nanocomposite Pr2Fe14B/α-Fe magnets by small substitution of M for Fe (M = Cr, Nb, Ti and Zr), J. Alloys Compd. 327 (2001) 201–205, https://doi.org/10.1016/S0925-8388(01)01418-9.
[60] C. Wang, M. Yan, W.Y. Zhang, Significant changes in the microstructure, phase transformation and magnetic properties of (Nd,Pr)2Fe14B/α-Fe magnets induced by Nb and Zr additions, Mater. Sci. Eng. B Solid State Mater. Adv. Technol. 123 (2005) 80–83, https://doi.org/10.1016/j.mseb.2005.07.002.
[61] A. Jianu, M. Valeanu, D.P. Lazar, F. Lifei, C. Bunescu, V. Pop, Effects of Zr and Ti substitutions on the crystallization processes of Fe3B/Nd2Fe14B nanocomposite magnetic system, J. Magn. Magn. Mater. 272–276 (2004) 1493–1494, https://doi.org/10.1016/j.jmmm.2003.12.1005.
[62] JEOL Ltd., Energy-dispersive X-ray spectroscopy, EDS, (n.d.). https://www.jeol.com/words/emterms/20121023.010500.php#gsc.tab=0 (accessed August 4, 2023).
[63] A. Cottrell, Solidification of Solutions and Impure metals, in: An Introd. to Metall., Second edi, Edward Arnold Ltd, 1995.
[64] Y. Matsuura, S. Hirosawa, H. Yamamoto, S. Fujimura, M. Sagawa, K. Osamura, Phase diagram of the nd-fe-b ternary system, Jpn. J. Appl. Phys. 24 (1985) 635–637, https://doi.org/10.1143/JJAP.24.L635.
[65] Y. Zhang, T. Ma, M. Yan, J. Jin, B. Wu, B. Peng, Y. Liu, M. Yue, C. Liu, Post-sinter annealing influences on coercivity of multi-main-phase Nd-Ce-Fe-B magnets, Acta Mater. 146 (2018) 97–105, https://doi.org/10.1016/j.actamat.2017.12.027.
[66] W.F. Li, T. Ohkubo, K. Hono, Effect of post-sinter annealing on the coercivity and microstructure of Nd–Fe–B permanent magnets, Acta Mater. 57 (2009) 1337–1346, https://doi.org/10.1016/J.ACTAMAT.2008.11.019.
[67] X. Liu, Y. Zhang, P. Zhang, T. Ma, M. Yan, L. Zhao, L. Li, Microstructure evolution of Dy69Ni31-added Nd-Fe-B sintered magnets during annealing, J. Magn. Magn. Mater. 486 (2019), 165260, https://doi.org/10.1016/J.JMMM.2019.165260.
[68] F. Vial, F. Joly, E. Nevalainen, M. Sagawa, K. Hiraga, K.T. Park, Improvement of coercivity of sintered NdFeB permanent magnets by heat treatment, J. Magn. Magn. Mater. 242–245 (2002) 1329–1334, https://doi.org/10.1016/S0304-8853(01)00967-2.
[69] S. Hirosawa, Y. Matsuura, Nd-Fe-B Permanent Magnet Materials, Jpn. J. Appl. Phys. 26 (1987) 785–800, https://doi.org/10.1143/JJAP.26.785.
[70] D. Tsai, T. Chin, S. Hsu, M. Hung, The phase diagrams of the pseudobinary Nd-(Fe 14 B) and the Fe-Nd-B ternary system, IEEE Trans. Magn. (1987) 3607–3609. http://ieeexplore.ieee.org/xpls/abs_all.jsp?arnumber=1065517.
[71] K.K. Kadyrzhanov, V.S. Rusakov, M.S. Fadeev, T.Y. Kiseleva, A.L. Kozlovskiy, I. E. Kenzhina, M.V Zdorovets, Study of Magnetic Properties of Fe(100-x)Ni(x) Nanostructures Using the Mössbauer Spectroscopy Method, Nanomater. (Basel, Switzerland). 9 (2019), https://doi.org/10.3390/nano9050757.
[72] H.Y. Wang, F.A. Zhao, N.X. Chen, G. Liu, Theoretical investigation on the phase stability of Nd2Fe14B and site preference of V, Cr, Mn, Zr and Nb, J. Magn. Magn. Mater. 295 (2005) 219–229, https://doi.org/10.1016/J.JMMM.2005.01.017.
[73] B. Yang, B.G. Shen, T.Y. Zhao, J.R. Sun, Significant improvements of structure and magnetic properties of Pr2Fe14B/α-Fe nanocomposite magnets due to Cu and Mn substitution, Mater. Sci. Eng. B 145 (2007) 11–16, https://doi.org/10.1016/J.MSEB.2007.09.047.
[74] C.S. Barret, T.B. Massalski, Structure of Metals, Pergamon P, Oxford, 1980.
[75] J. Wang, Y. Meng, H. Zhang, H. Tang, R. Lin, C. Sun, C. Wu, F. Xie, The characteristic of crystal growth of Nd–Fe–B cast strips during the rapid solidification process, J. Magn. Magn. Mater. 396 (2015) 283–287, https://doi.org/10.1016/J.JMMM.2015.08.004.
[76] H. Sepehri-Amin, Y. Une, T. Ohkubo, K. Hono, M. Sagawa, Microstructure of fine-grained Nd–Fe–B sintered magnets with high coercivity, Scr. Mater. 65 (2011) 396–399, https://doi.org/10.1016/J.SCRIPTAMAT.2011.05.006.
[77] T. Tomše, J. Jaćimović, L. Herrmann, F. Greuter, R. Simon, S. Tekavec, J. M. Dubois, S. Kobe, Properties of SPS-processed permanent magnets prepared from gas-atomized Nd-Fe-B powders, J. Alloys Compd. 744 (2018) 132–140, https://doi.org/10.1016/J.JALLCOM.2018.01.411.
[78] K. Hioki, A. Hattori, T. Iriyama, Development of Dy-free hot-deformed Nd-Fe-B magnets by optimizing chemical composition and microstructure, J. Magn. Soc. Jpn. 38 (2014) 79–82, https://doi.org/10.3379/msjmag.1404r001.
[79] X.G. Cui, M. Yan, T.Y. Ma, W. Luo, S.J. Tu, Design and fabrication of sintered Nd-Fe-B magnets with a low temperature coefficient of intrinsic coercivity, Sci. Sinter. 41 (2009) 91–99, https://doi.org/10.2298/SOS0901091C.
[80] M.D. Calin, E. Helerea, Temperature influence on magnetic characteristics of NdFeB permanent magnets, in: Proceedings of the 2011 7th International Symposium on Advanced Topics in Electrical Engineering (ATEE) 2011, 2011.